Article

Cell Reports

A Highly Conserved Circular RNA Is Required to Keep Neural Cells in a Progenitor State in the Mammalian Brain

Graphical Abstract

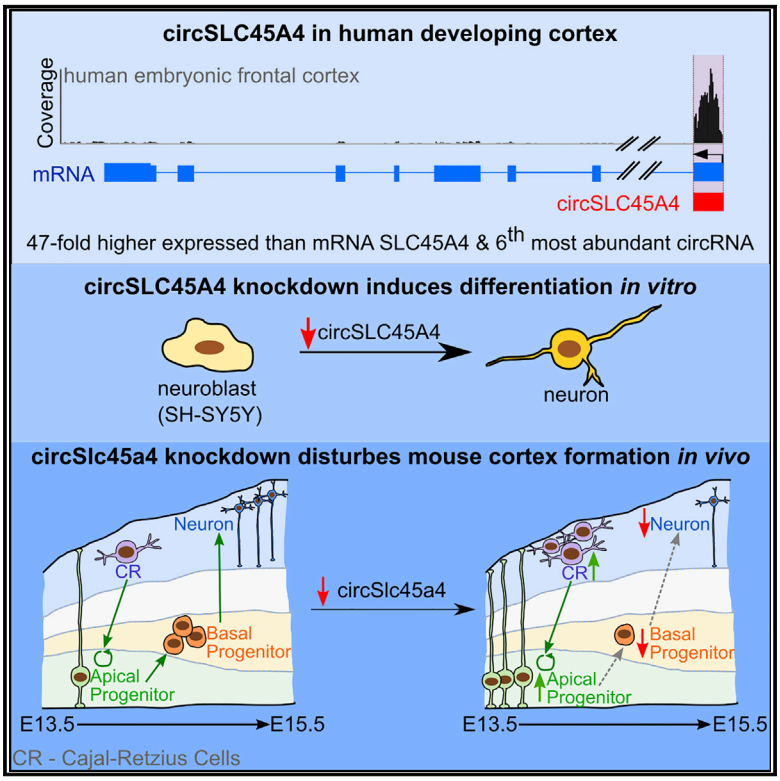

Highlights

- circSLC45A4 is the 6th highest expressed circRNA in human fetal (22 weeks) cortex
- Knockdown of circSLC45A4 in human SH-SY5Y cells causes spontaneous differentiation
- circSlc45a4 knockdown depletes the basal progenitor pool in developing mouse cortex

Authors

Christin Suenkel, Daniel Cavalli, Simone Massalini, Federico Calegari, Nikolaus Rajewsky

Correspondence

federico.calegari@tu-dresden.de (F.C.), rajewsky@mdc-berlin.de (N.R.)

In Brief

Suenkel et al. present a detailed study of the highly conserved circular RNA (circRNA) circSLC45A4 in human neuroblastoma cells and mouse embryonic cortex. They use perturbation experiments and RNA-seq to demonstrate that circSLC45A4 is required to keep neural cells in a progenitor state.

Suenkel et al., 2020, Cell Reports *30*, 2170–2179
February 18, 2020
https://doi.org/10.1016/j.celrep.2020.01.083

CellPress

OPEN ACCESS
CellPress

Cell Reports
Article

A Highly Conserved Circular RNA Is Required to Keep Neural Cells in a Progenitor State in the Mammalian Brain

Christin Suenkel,[1] Daniel Cavalli,[2] Simone Massalini,[2] Federico Calegari,[2,*] and Nikolaus Rajewsky[1,3,*]
[1]Berlin Institute for Medical Systems Biology, Max Delbrück Center for Molecular Medicine within the Helmholtz Association, Systems Biology of Gene Regulatory Elements, Hannoversche Straße 28, 10115 Berlin, Germany
[2]CRTD-Center for Regenerative Therapies Dresden, TU Dresden, Fetscherstraße 105, 01307 Dresden, Germany
[3]Lead Contact
*Correspondence: federico.calegari@tu-dresden.de (F.C.), rajewsky@mdc-berlin.de (N.R.)
https://doi.org/10.1016/j.celrep.2020.01.083

SUMMARY

circ*SLC45A4* is the main RNA splice isoform produced from its genetic locus and one of the highest expressed circRNAs in the developing human frontal cortex. Knockdown of this highly conserved circRNA in a human neuroblastoma cell line is sufficient to induce spontaneous neuronal differentiation, measurable by increased expression of neuronal marker genes. Depletion of circ*Slc45a4* in the developing mouse cortex causes a significant reduction of the basal progenitor pool and increases the expression of neurogenic regulators. Furthermore, knockdown of circ*Slc45a4*a induces a significant depletion of cells in the cortical plate. In addition, deconvolution of the bulk RNA-seq data with the help of single-cell RNA-seq data validates the depletion of basal progenitors and reveals an increase in Cajal-Retzius cells. In summary, we present a detailed study of a highly conserved circular RNA that is necessary to maintain the pool of neural progenitors *in vitro* and *in vivo*.

INTRODUCTION

Circular RNAs (circRNAs) are a class of RNA molecules that are formed by head-to-tail splicing (also known as backsplicing), in which a downstream 5′ splice site (SS) is covalently connected to an upstream 3′ SS of an RNA molecule (Ashwal-Fluss et al., 2014; Hansen et al., 2013; Ivanov et al., 2015; Memczak et al., 2013; Salzman et al., 2012; Starke et al., 2015; Zhang et al., 2014). Furthermore, circRNAs are widely conserved and abundantly expressed (Hansen et al., 2013; Maass et al., 2017; Memczak et al., 2013; Salzman et al., 2013; Wang et al., 2014), especially in neural tissues (Maass et al., 2017; Rybak-Wolf et al., 2015; You et al., 2015). Although thousands of circRNAs have been reported, only a few examples of their function exist. CDR1as, for example, mediates miR-7 efficacy in the center of a RNA regulatory network in the mammalian brain (Kleaveland et al., 2018; Piwecka et al., 2017), circZnf609 and circMbl encode small peptides (Legnini et al., 2017; Pamudurti et al., 2017), and circFoxo3 regulates the assembly of a protein complex that controls cell-cycle progression (Du et al., 2016).

We previously showed that circRNAs are abundantly expressed in neural samples, predominantly localized at the synaptoneurosomes, and are expressed in a spatiotemporally controlled manner (Rybak-Wolf et al., 2015; You et al., 2015). However, their functional involvement in neural development remains elusive. Consequentially, to date, no circRNA has been identified as a regulator of nervous system development.

A widely used model system for studying the mechanisms of the development of the nervous system is the developing mouse cortex. Here, many different processes must be coordinated in space and time to allow the successful generation of neurons (NEUs) from neural stem and progenitor cells (Götz and Huttner, 2005; Mora-Bermúdez et al., 2013; Noctor et al., 2007; Sun and Hevner, 2014). To form the 6 layers of the mammalian neocortex, neurogenesis must be followed by neuronal migration, neuronal differentiation, dendrogenesis, axogenesis, and synaptogenesis, and the formation of connections (Komuro and Rakic, 1998; Kriegstein and Noctor, 2004). However, any kind of misregulation of these well-orchestrated processes can prevent the proper formation of the developing cortex. Neuroepithelial cells appear before neurogenesis in the developing cortex and form a single cell layer at the apical surface, the neuroepithelium. After the start of neurogenesis, neuroepithelial cells give rise to radial glial cells. Radial glial cells are already more fate restricted and, like neuroepithelial cells, exhibit apical-basal polarity (Götz and Huttner, 2005). Radial glial and neuroepithelial cells are referred to as apical progenitors (APs), and at early stages of cortical development, they expand their pool by symmetric proliferative divisions. When neurogenesis begins, APs progressively switch to asymmetric divisions, giving rise to basal progenitors (BPs; i.e., basal intermediate progenitors and basal radial glia) and NEUs (Florio and Huttner, 2014). These neural progenitors primarily undergo symmetric neurogenic divisions and constitute the main source of NEUs in mice. Newborn NEUs migrate in waves to the pial surface of the brain across the intermediate zone and settle down in the cortical plate (CP), where they mature and form synaptic connections with one another (Angevine and Sidman, 1961; Götz and Huttner, 2005; Gupta et al., 2002; Paridaen and Huttner, 2014; Taverna et al., 2014). In addition, post-mitotic NEUs in the upper cortical layers can influence the progenitor cells in this system (Paridaen and Huttner, 2014).

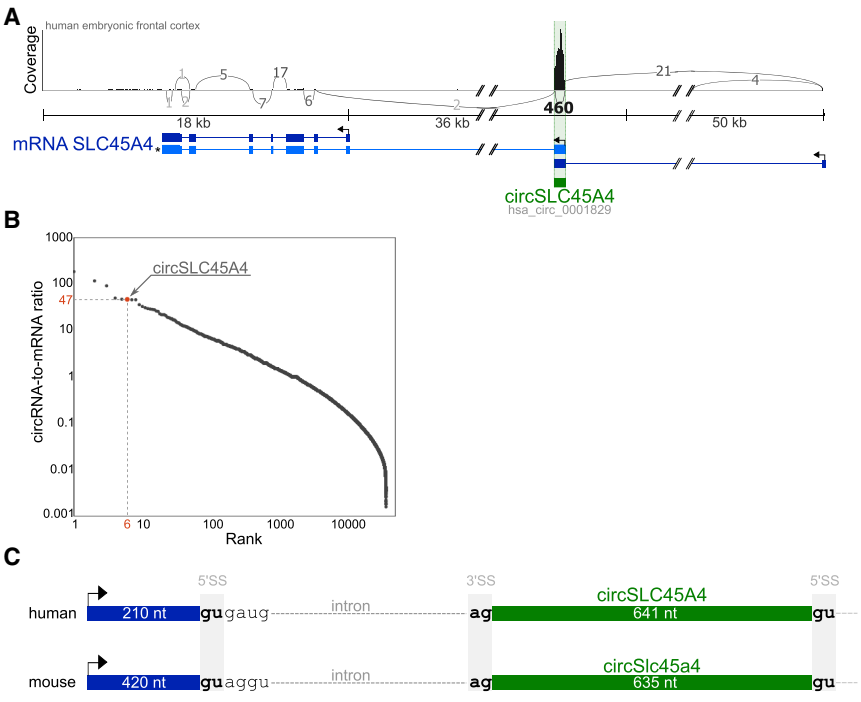

Figure 1. circ*SLC45A4* Is a Conserved circRNA That Is Highly Expressed in Human Embryonic Frontal Cortex

(A) Genetic locus of circ*SLC45A4* in humans. mRNA isoform shown in blue, circRNA in green. The circRNA is produced from an alternative first exon (light blue, *) that sometimes is also included in the mRNA. The coverage track shows total RNA sequencing of fetal human cortex, 22 weeks, ENCODE: ENCSR000AEY. The numbers on the connecting lines indicate the number of reads supporting the splice junction. The location of circ*SLC45A4* (hsa_circ_0001829) is indicated.

(B) Expression rank of circ*SLC45A4* in fetal human cortex, ranked by circRNA:mRNA ratio (6th, top 0.02%).

(C) Splice sites that facilitate the production of circ*SLC45A4* in human and mouse are conserved. See also Figure S1.

It was shown that Cajal-Retzius cells, a neuron type born very early in the neocortex, dynamically regulate AP maintenance and the switch to neurogenesis and gliogenesis in the neocortex (Lakomá et al., 2011). Although a plethora of proteins (Taverna et al., 2014) and long noncoding RNAs (Aprea and Calegari, 2015) have been implicated in the regulation of corticogenesis, the role of circular RNAs in this complex process remains elusive.

Here, we identify a circRNA, circ*SLC45A4*, that is highly conserved between human and *Xenopus tropicalis* and is one of the highest expressed circRNAs in the human embryonic frontal cortex at gestational week 22. We show that knockdown (KD) of circ*SLC45A4* is sufficient to induce spontaneous neuronal differentiation in human neuroblastoma cells (SH-SY5Y). In addition, *in vivo* KD of this circRNA in the developing mouse cortex significantly reduces the pool of BPs and ultimately decreases the number of NEUs residing in the CP. High-throughput RNA sequencing (RNA-seq) revealed the strong and significant upregulation of several neurogenic factors, such as Notch2, Foxp2, and Unc5b. Cell-type proportions were estimated computationally from bulk RNA-seq data with the help of single-cell RNA-seq data and not only confirms the depletion of the BP pool but also indicates an increase in the number of Cajal-Retzius cells.

RESULTS

circ*SLC45A4* Is a Highly Conserved circRNA That Is Highly Expressed in Human Embryonic Frontal Cortex

Previously, we created a catalog of circRNAs expressed in neural samples, which highlighted their abundant expression, conservation, predominant localization to the synaptoneurosomes, and spatiotemporally controlled expression (Rybak-Wolf et al., 2015). This collection of neural circRNAs included many molecules that are implicated in neuronal differentiation, but their mode of action is not yet understood. This catalog included circ*SLC45A4*, a circRNA that is produced from an alternative 1st exon of *SLC45A4* (Figure 1A). It stood out for its dynamic spatial expression pattern in different brain regions (Rybak-Wolf et al., 2015). *SLC45A4* encodes a proton-dependent sugar transporter that can recognize glucose, fructose, and sucrose as substrates and was shown to be important in spermatozoa nutrition (Vitavska and Wieczorek, 2017). However, the function of circ*SLC45A4* remains elusive, as it has never been studied in any biological context.

To survey circRNA expression in development, we analyzed a total RNA-seq dataset of human embryonic frontal cortex at gestational week 22, collected by the ENCODE consortium (ENCODE Project Consortium, 2012). This dataset surprisingly revealed that circ*SLC45A4* is the main RNA splice isoform from its genomic locus (Figure 1A) and overall one of the highest expressed circRNAs in the human cortex at that developmental time point. Among all of the circular RNAs expressed in that dataset, circ*SLC45A4* is ranked 6th of 36,408 (top 0.02%) by the circRNA:mRNA ratio (circRNA 47 times higher than mRNA). Considering just the reads spanning the circRNA specific head-to-tail junction (460 total) (httj), circ*SLC45A4* would still be among the top 1% highly expressed circRNAs in the developing human cortex (Figure S1A), rendering this particular circRNA a highly interesting candidate to study in the context of neuronal development. This ENCODE dataset also revealed an unannotated upstream exon that is necessary to facilitate the formation of circ*SLC45A4* by a splicing reaction. Not only is this upstream exon present in humans and mice (Figure 1C), but the mouse upstream exon is also exactly duplicated in length (420 nt instead of 210 nt in humans) and the SSs are conserved. To further assess the conservation, we turned to the PhyloP score (Pollard et al., 2010), which is the per base conservation based on the alignment of 100 vertebrates. This shows that the

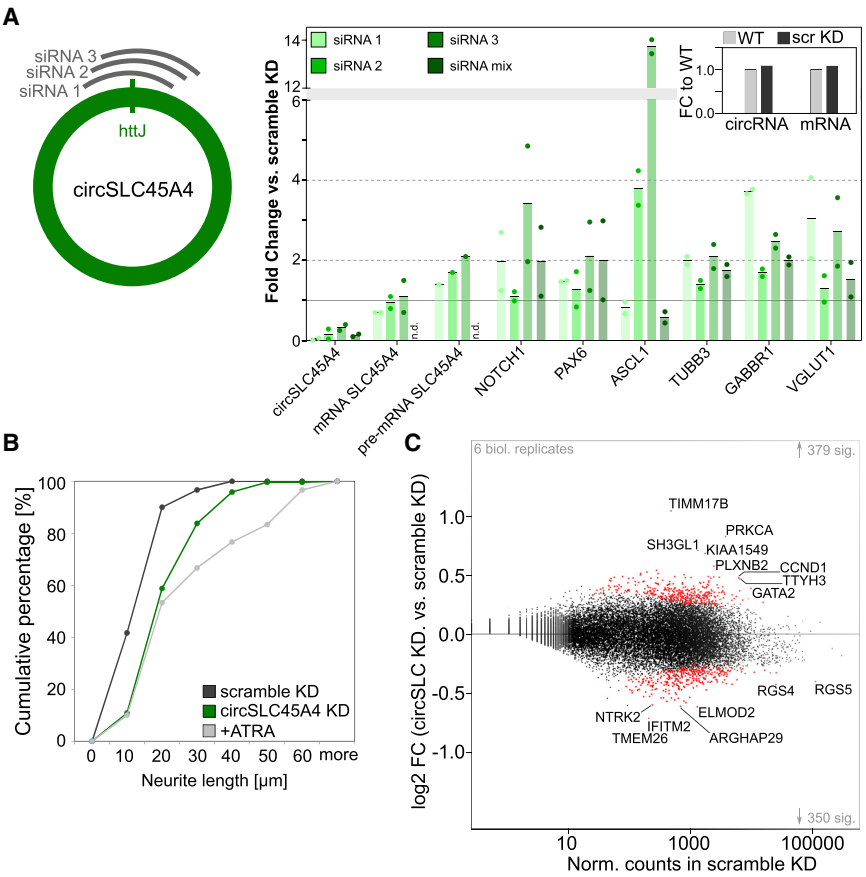

Figure 2. Knockdown (KD) of circ*SLC45A4* in the Human Neuronal Cell Line SH-SY5Y Cells Causes Spontaneous Differentiation

(A) siRNA design strategy for circ*SLC45A4*-specific KD and qPCR measurements after KD of circ*SLC45A4* in SH-SY5Y cells, each dot indicating a separate biological replicate (n = 2), the vertical lines marking the averages of the replicates. Fold changes are compared to scramble KD, the baseline is marked as horizontal line at fold change 1. n.d., not determined. Inset shows the effect of scramble KD on circ*SLC45A4* (+7.4%) or mRNA *SLC45A4* (+7.2%) expression levels compared to wild type.

(B) Results of neurite length measurements after circ*SLC45A4* KD, scramble KD, and differentiation with all-*trans* retinoic acid (ATRA). All neurites of 30 cells per condition counted.

(C) MA plot of circ*SLC45A4* KD versus scramble KD. 6 biological replicates, 2 for each siRNA, are considered. Significant fold changes are highlighted in red, if adjusted $p < 0.05$ (Wald test, p value adjusted with Benjamini-Hochberg method).

See also Figure S2 and Table S1.

circRNA-forming exon of *SLC45A4* is significantly more conserved than the 8th exon of this gene, containing coding sequences (CDSs) and 3′ UTR, but that it is also significantly more conserved than the 1st exons of genes from the same gene family (SLC45Ax) (Figure S1B). This locus is exhibiting unusually strong sequence conservation in the circRNA-containing parts. circ*SLC45A4* is highly conserved on the nucleotide level between humans and *X. tropicalis,* exhibiting 65.8% sequence identity (Figure S1C). Only 0.94% (6 of 641 nt) of the human to *X. tropicalis* alignment in that region belongs to a gap. In contrast, the 3′ UTR and intronic regions of this gene are much less conserved (Figure S1D). In *X. tropicalis*, only 43% of this region shows sequence identity with humans. This may suggest that the circRNA-containing part of *SLC45A4* is under a stronger selection pressure than other regions of this gene.

Knockdown of circ*SLC45A4* in the Human Neuronal Cell Line SH-SY5Y Cells Causes Spontaneous Differentiation

Next, we sought to explore the effects of perturbing circ*SLC45A4* in a human model system of neuronal differentiation. SH-SY5Y cells are a widely used human cell line to study neuronal differentiation (Kovalevich and Langford, 2013; Ross et al., 1983). Through 2-color single-molecule fluorescence *in situ* hybridization (FISH) (Raj and Tyagi, 2010), we detected an average of 3.7 and 8.8 molecules of circ*SLC45A4* and mRNA per SH-SY5Y cell, respectively (Figure S2A). Fractionation experiments revealed that the circRNA is localized predominantly in the cytoplasm, while the mRNA is also found in nuclear and mitochondrial fractions (Figure S2B). Following the expression of circ*SLC45A4* and its corresponding mRNA over the course of all-*trans* retinoic acid (ATRA)-induced differentiation of SH-SY5Y (Påhlman et al., 1984; Ross et al., 1983) and of a 2nd human neuronal cell line, NTERA-2 (Lee and Andrews, 1986; Pleasure and Lee, 1993), revealed that the expression of circ*SLC45A4* peaks at the time of neuronal lineage commitment or birth of young NEUs (Figure S2C). Next, we conducted perturbation experiments of circ*SLC45A4* levels by small interfering RNA (siRNA)-mediated KD in SH-SY5Y cells (Elbashir et al., 2001). Three independent siRNAs that target the httj of the circular RNA are used. They are shifted with respect to one another by a few nucleotides to ensure that if they had off-target effects, then they would differ one from another. Accordingly, the KD results for each siRNA were evaluated independently and only called true positives if they were observed after separate treatment with all 3 siRNAs (Figure 2A). circ*SLC45A4* was efficiently downregulated by 60%–99%, as compared to a non-targeting scramble siRNA (Figure 2A). To ensure that the scramble siRNA did not have any effects on the expression level of circ*SLC45A4* or mRNA *SLC45A4*, we compared their levels to wild-type expression levels. After treatment of SH-SY5Y cells with scramble siRNA, circRNA and mRNA levels were increased by 7% (Figure 2A, inset). qPCR analysis of the genes involved in neuronal commitment (NOTCH1, PAX6, ASCL1) and genes marking newborn or more mature NEUs (TUBB3, GABBR1, VGLUT1) revealed their upregulation by 2- to 14-fold (Figure 2A), indicating that KD of circ*SLC45A4* alone is sufficient to induce spontaneous neuronal differentiation (Figure 2A). The induction of neuronal differentiation was further supported by increased expression of TUBB3 protein in SH-SY5Y,

while glial fibrillary acidic protein (GFAP), a marker for astrocyte differentiation, was not induced (Figures S2D and S2E). Taking all of the previous results into account, they indicate that KD of circ*SLC45A4* alone is sufficient to induce spontaneous neuronal differentiation, which is corroborated by the increased neurite length of SH-SY5Y cells after circ*SLC45A4* KD (+7.9 μm average neurite length) (Figure 2B). To ensure that these effects were not caused by a stress response, an identical KD approach was applied to other unrelated but similarly expressed circRNAs (circ*VAPA*, circ*CPSF6*, circ*ZNF609*), which resulted in no detectable effects concerning neuronal differentiation (data not shown).

These findings prompted us to investigate transcriptome-wide changes induced by circ*SLC45A4* KD. PolyA+ RNA-seq confirmed a significant induction of neuronal genes (Figure 2C), including PRKCA, PLXNB2, BSN, SEMA5B, and SHANK1. Gene Ontology (GO) term analyses of significantly up- and downregulated genes supported this observation (Table S1) and additionally indicated the transcriptome-wide upregulation of genes involved in cell adhesion and histone methylation after KD of circ*SLC45A4*.

Knockdown of circ*Slc45a4* Depletes the BP Pool in the Developing Mouse Cortex

In vitro cell culture models such as SH-SY5Y cells have the advantage that a complex process like neurogenesis can be analyzed in a simplified system. However, this is also one of their main limitations, as these *in vitro* models lack multiple features that are important in complex tissues or developing organisms—for example, 3-dimensional cell-cell interactions, tissue polarity, and complex temporal and spatial regulation of differentiation processes.

To characterize the effect of circ*Slc45a4* in a more physiologically relevant system, we investigated the expression of circ*Slc45a4* during mouse brain development (Figure 3A). circ*Slc45a4* shows the highest expression in the adult mouse brain, but during development, expression peaks were detected at embryonic day (E) 16.5 and at postnatal day 3. The 1st peak of circ*Slc45a4* expression coincides with the peaks of neurogenesis in the nucleus accumbens, tufted cells, and isle of Calleja, and the formation of the corpus callosum and the neurogenesis in cortical layer IV (Finlay and Darlington, 1995). BaseScope is an *in situ* hybridization method that permits the detection of specific SSs (ACDBio) and has previously been used to successfully stain circRNAs (Piwecka et al., 2017). Hence, it was used to further assess the in-tissue distribution of circ*Slc45a4*. E15.5 mouse cortices were stained for circ*Slc45a4* and mRNA *Slc45a4* (Figure 3B). The expression of circ*Slc45a4* and mRNA *Slc45a4* was detected across all cortical layers, suggesting a general role for these molecules. This observation and the fact that circ*Slc45a4* is upregulated in differentiating progenitors and NEUs compared to proliferating progenitors at E14.5 (Aprea et al., 2013; Dori et al., 2019) led us to perturb the levels of both circular and mRNA *Slc45a4* in the developing neocortex. Thus, we proceeded with *in utero* electroporation experiments at E13.5 to target both proliferating and differentiating progenitors before the observed peak of circRNA expression at E16.5. Here, plasmids encoding a short hairpin RNA (shRNA) specific to either circ*Slc45a4* (3 different shRNAs), mRNA *Slc45a4* (2 different shRNAs), or a scramble shRNA that are co-expressing a nuclear GFP reporter were injected in the ventricle of E13.5 mouse embryos. The constructs were then electroporated into the cells of the ventricular zone (VZ) of the developing lateral cortex. GFP+ cells were sorted using fluorescence-activated cell sorting (FACS) 48 h post-electroporation. qPCR analysis revealed that circ*Slc45a4* was depleted by 80%, while the mRNA was slightly downregulated by 25%. The shRNAs against mRNA *Slc45a4* depleted it by 50% and left the circ*Slc45a4* levels unaffected (Figures 3C and 3D). We used mixes of several shRNAs for the *in utero* electroporation and KD after validating that each shRNA was specific to the intended target in a mouse cell line (P19) (Figure S3A). Hence, the observed downregulation of mRNA *Slc45a4* after KD of circ*Slc45a4* is probably a secondary effect. Quantification of GFP+ cells (electroporated) in the different cortical layers revealed a significant depletion of cells from the CP for both circRNA and mRNA KD (Figures 3E and 3F). After KD of the circRNA, we observed a significant depletion of cells from the subventricular zone (SVZ) (Figure 3F). This was not the case after KD of mRNA *Slc45a4*. Next, we quantified the proportions of APs, BPs, and NEUs, defined by cellular localization in the cortex and expression of Tbr2, the main marker of BPs (Englund et al., 2005). This analysis revealed a significant depletion of BPs (Tbr2+ in VZ and SVZ), as well as a significant increase in APs (Tbr2− in VZ) after KD of circ*Slc45a4* compared to scramble KD (Figures 3G and S3B). Pax6 was further used to identify APs and Ctip2 to identify deep-layer NEUs, which supported the previously observed increase in AP and reduced neurogenesis (Figures S3C–S3E). The proportion of Tbr2+ cells among electroporated cells was significantly affected only in the VZ and not in the SVZ (Figure 3H), indicating that circSLC45a4 KD specifically impaired the cell-fate switch from AP to BP. We did not observe this effect after KD of mRNA *Slc45a4*.

Knockdown of circ*Slc45a4* Induces Significant Transcriptomic Changes in the Developing Mouse Cortex

Subsequently, we aimed to gain more insight into the molecular mechanism caused by circ*Slc45a4* KD in the developing cortex by RNA-seq analysis of manipulated cells. The plasmids used for *in vivo* KD of circ*Slc45a4*, mRNA *Slc45a4*, and scrambled control also carried a GFP marker to be able to track manipulated cells *in vivo*. Furthermore, this enabled the purification of electroporated cells from E15.5 embryonic mouse cortices by FACS. RNA was extracted from the cells and used to prepare polyA+ RNA-seq libraries. Analysis of the gene expression changes induced after circ*Slc45a4* KD versus scramble KD revealed expression changes of up to 16-fold induction or 8-fold downregulation of many genes (Figure 4A), some of which were validated by qPCR (Figures S4B and S4C).

Next to controlling the effects of the shRNA KD by electroporation of a scrambled shRNA, we also used a construct against mRNA *Slc45a4*. This served 2 purposes: (1) targeting an expressed RNA to rule out that the observed effects are caused by overloading Dicer or depleting AGO2 and (2) targeting the corresponding mRNA to ensure that the molecular consequences are due to the manipulation of the circular RNA. If that was not the case, one would expect to find similar changes after KD of circ*Slc45a4* and mRNA *Slc45a4*. However, principal-component analysis (PCA) shows that circ*Slc45a4* and mRNA

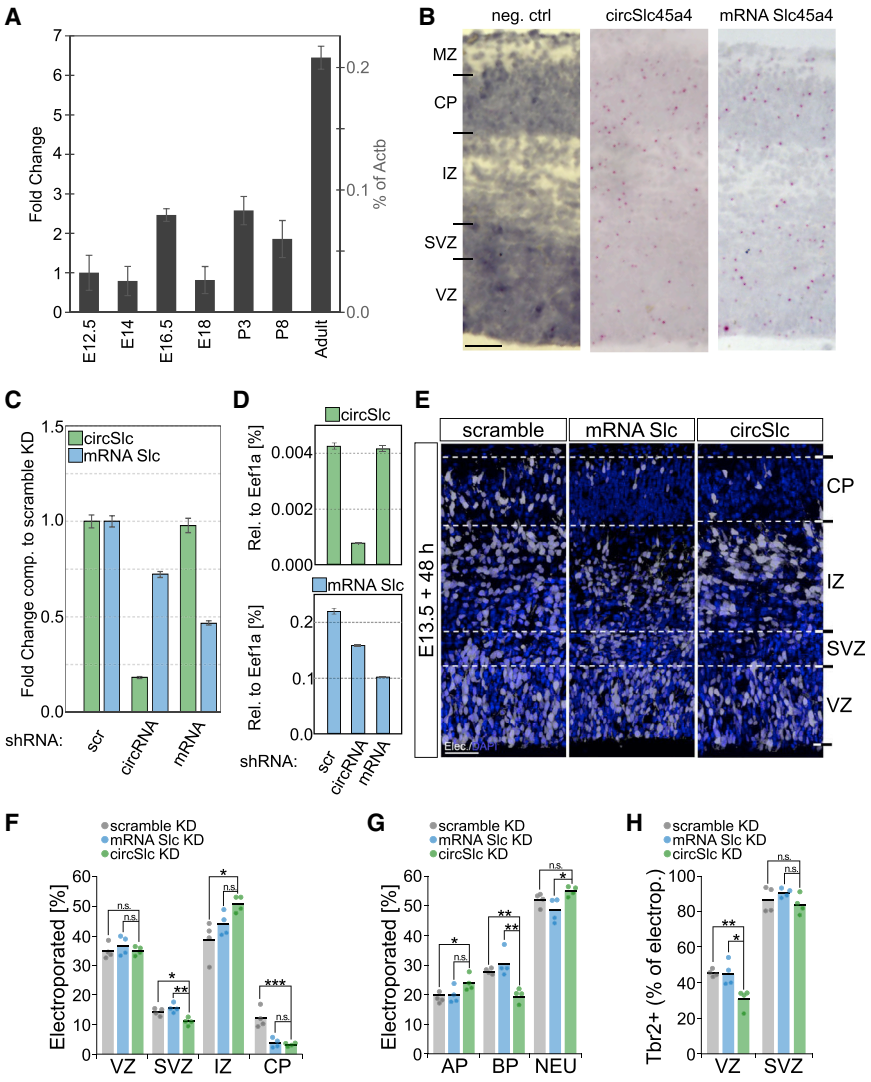

Figure 3. KD of circ*Slc45a4* Depletes the Basal Progenitor (BP) Pool in the Developing Mouse Cortex

(A) Expression levels of circ*Slc45a4* in developing whole mouse brain as determined by qPCR. Error bars are SD from 3 technical replicates.

(B) Splice site-specific *in situ* hybridization of circ*Slc45a4* and mRNA *Slc45a4*. Probe against bacterial *DapB* as negative control. CP, cortical plate; IZ, intermediate zone; MZ, marginal zone; SVZ, subventricular zone; VZ, ventricular zone. Scale bar, 50 μm.

(C and D) KD efficiency of *in utero* electroporation. Determined by qPCR, 3 biological replicates, shRNA construct mixes were used per replicate. Error bars indicate SEMs. (C) Fold Change compared to scramble KD, normalized by Eef1a. (D) Relative expression levels of circSlc45a4 and mRNA Slc45a4 versus Eef1a.

(E) Manipulated cells (white, GFP+) in developing cortex at E15.5 for scrambled control KD, mRNA *Slc45a4*, and circ*Slc45a4* KD. Nuclei are DAPI stained (blue). Scale bar, 50 μm.

(F) Cell distribution per cortical zone; 4 biological replicates.

(G) Percentage of electroporated cells that are classified as APs, BPs, and neurons (NEUs) by Tbr2+ staining and localization.

(H) Percentage of BPs in VZ and SVZ after scramble, circRNA, or mRNA KD.

(F–H) *p < 0.05, **p < 0.01; n.s., not significant, t test. See also Figure S3.

Informing the Bulk RNA-Seq Data with a Single-Cell Dataset Confirms the Depletion of BPs and Reveals an Increase in Cajal-Retzius Cells

A few of the observed up- and downregulated genes may be false positives, as the initial composition of cell types considered in this analysis were different (i.e., in the scramble KD, cells from all layers are present; in circ*Slc45a4* KD the CP and the SVZ are less populated). For example, the downregulation of Cux2 could be explained by the absence of cells from the CP in mRNA and circRNA KD compared to the scramble KD.

Slc45a4 KD in the developing mouse cortex varied from each other and the scramble KD (Figure 4B). Furthermore, comparison of circ*Slc45a4* KD versus scramble KD with circ*Slc45a4* KD versus mRNA *Slc45a4* KD reveals that the changes induced by circ*Slc45a4* KD are stable and that these 2 comparisons are positively correlated (R^2 = 0.6975, Pearson) (Figures 4C and S4A). Again, the obtained bulk RNA-seq data were used for a GO term enrichment analysis to identify affected biological processes (Table S2). Genes connected to signaling, cell communication, adhesion, and regulation of development are upregulated, while genes implied in multiple biosynthetic pathways are downregulated. One of the main differences between apical and BPs is their attachment to the apical surface of the cortex. Newborn BPs delaminate from the apical adherens junction belt (Wilsch-Bräuninger et al., 2016). Hence, finding the genes upregulated after circ*Slc45a4* KD significantly overrepresented in cell adhesion and biological adhesion is in agreement with our previous observation that the number of APs is significantly increased and the number of BPs decreased.

Hence, Bseq-SC (Baron et al., 2016), a bioinformatics pipeline that takes single-cell RNA-seq data to inform bulk RNA-seq, was used to assess changes on cell-type levels. Bseq-SC can estimate cell-type proportions in bulk RNA-seq data based on cell-type definitions. These cell-type definitions are based on gene expression (e.g., marker genes, sets of marker genes). Subsequently, the effects on the measured gene expression caused by changes in cell-type proportions and by the KD of the circRNA or mRNA itself could be deconvolved (Figure 5A). We used pre-existing single-cell RNA-seq data that were not collected as part of this study (Yuzwa et al., 2017). Yuzwa and colleagues assessed different time points of cortical development in embryonic mice of the same strain that was used in the present study. First, the Yuzwa et al. data were reanalyzed

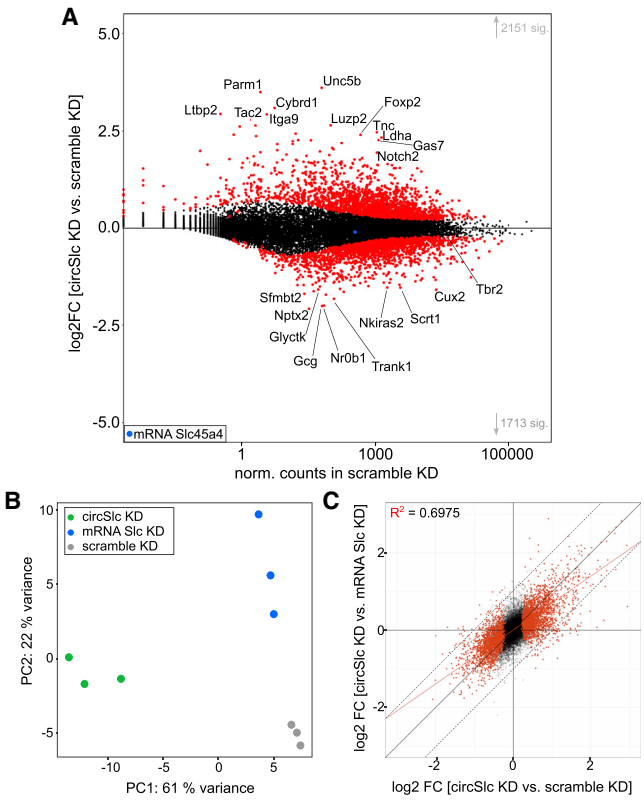

Figure 4. KD of circ*Slc45a4* Induces Strong Transcriptomic Changes in the Developing Cortex

(A) MA plot of 3 biological replicates of circ*Slc45a4* KD in mouse cortex versus scrambled KD. A total of 2,151 genes are significantly (p-adj < 0.01) upregulated and 1,713 are significantly (p-adj < 0.01) downregulated and are highlighted in red. Tbr2 as BP marker is highlighted (log2 FC = −0.41, p-adj = 8.63×10^{-6}). Wald test, p value adjusted with Benjamini-Hochberg method.

(B) Principal-component analysis (PCA) separates the 3 measured conditions.

(C) Comparison of circ*Slc45a4* KD versus scramble KD with circ*Slc45a4* KD versus mRNA *Slc45a4* KD shows a positive correlation ($R^2 = 0.6975$, Pearson, red line). Genes that were found to be significantly changed in circ*Slc45a4* versus scramble KD (compare to A) are highlighted in red. Dashed gray lines mark the area where log2 FC in both comparisons are below 1.

See also Figure S4 and Table S2.

using Seurat (Butler et al., 2018). The t-distributed stochastic neighbor embedding (tSNE) plot for E15.5 illustrates the 14 identified cell types (Figure S5A). Specific marker genes for these 14 cell types were identified and assessed for being exclusively expressed in a single cell type and only marginally in any other cell type (Figure S5B). The cluster identity was determined with literature research for described functions of the selected markers. The unique gene expression sets determined for the different cell types present in the cortex at that developmental time point were then used to estimate cell-type proportions in the bulk RNA-seq data (Figure 5B). This analysis confirmed the previous observation that BPs are significantly depleted after KD of circ*Slc45a4*. We previously found BPs to be unaffected after the KD of mRNA *Slc45a4* and again could confirm it with this analysis (Figure 5C). In addition, this analysis revealed that the number of Cajal-Retzius cells, a type of reelin-producing NEU, significantly increased after KD of circ*Slc45a4* but was unaffected by perturbation of mRNA *Slc45a4*. This prediction from single-cell RNA-seq and bulk RNA-seq data was further assessed qualitatively with an immunostaining of embryonic mouse brains at E15.5 after KD of circ*Slc45a4*, mRNA *Slc45a4*, or scramble control. We find an increased expression of reelin only after KD of circ*Slc45a4*, which indicates an increase in the number of Cajal-Retzius cells (Figure S5C). KD of the mRNA is predicted to lead to an increase in the number of subcortical projection NEUs and neural stem and/or progenitor cells (Figures 5B and 5C). These results suggest that although both transcript isoforms are produced from the same genetic locus, the molecular pathways they are involved in to regulate corticogenesis are substantially different.

DISCUSSION

In the present work, we identified circ*SLC45A4* as the highest expressed isoform from its genetic locus in developing human cortex, at gestational week 22. At gestational week 22, neurogenesis in the cortex is almost completed, while neuronal migration and maturation are only beginning (Stagni et al., 2015). In addition, we measured circ*Slc45a4* levels in the whole mouse brain and found its expression to peak at E16.5, a time point at which neurogenesis in the mouse brain is peaking in many mouse brain regions (Finlay and Darlington, 1995) and at which upper-layer NEUs are formed in the cortex (Mihalas et al., 2016). With this indication of circ*SLC45A4* playing a role in neurogenesis, we perturbed its expression level by siRNA-mediated RNAi (Elbashir et al., 2001) in a widely used human model system for neuronal differentiation (SH-SY5Y) and in the developing mouse cortex. In SH-SY5Y cells, we observed spontaneous neuronal differentiation following circ*SLC45A4* KD. In the mouse cortex, we observed a specific depletion of the BP pool, while more Cajal-Retzius cells seemed to be produced. We had selected E13.5 to E15.5 for *in vivo* manipulations, reasoning that KD of circ*Slc45a4* before its expression peak should increase the changes and magnitude of the observed phenotype.

We have used siRNAs (SH-SY5Y cells) and shRNAs (mouse cortex) to manipulate the levels of circ*SLC45A4*. Perturbations involving siRNAs or shRNAs require stringent controls to ensure that the observed effects are indeed caused by KD of the target and not off-targets or unspecific consequences of the experiment. To control for potential immunogenic effects, we used a scramble control that does not target any known transcript. In addition, we included the KD of the *SLC45A4* mRNA as a control that served 2 purposes: (1) to rule out that the observed phenotype is a consequence of changing the stoichiometry of the endogenous RNAi machinery when targeting an expressed transcript and (2) to verify that the consequences of the circRNA perturbation are different from the mRNA perturbation. Furthermore, we are well aware that siRNAs and shRNAs are prone to have off-target effects, either by downregulation of unintended targets, by functioning as miRNAs, or by overloading Dicer and thereby impairing its function or depleting the effective AGO2 concentration. To minimize this risk, several precautions were taken: (1) several independent siRNAs against the same target

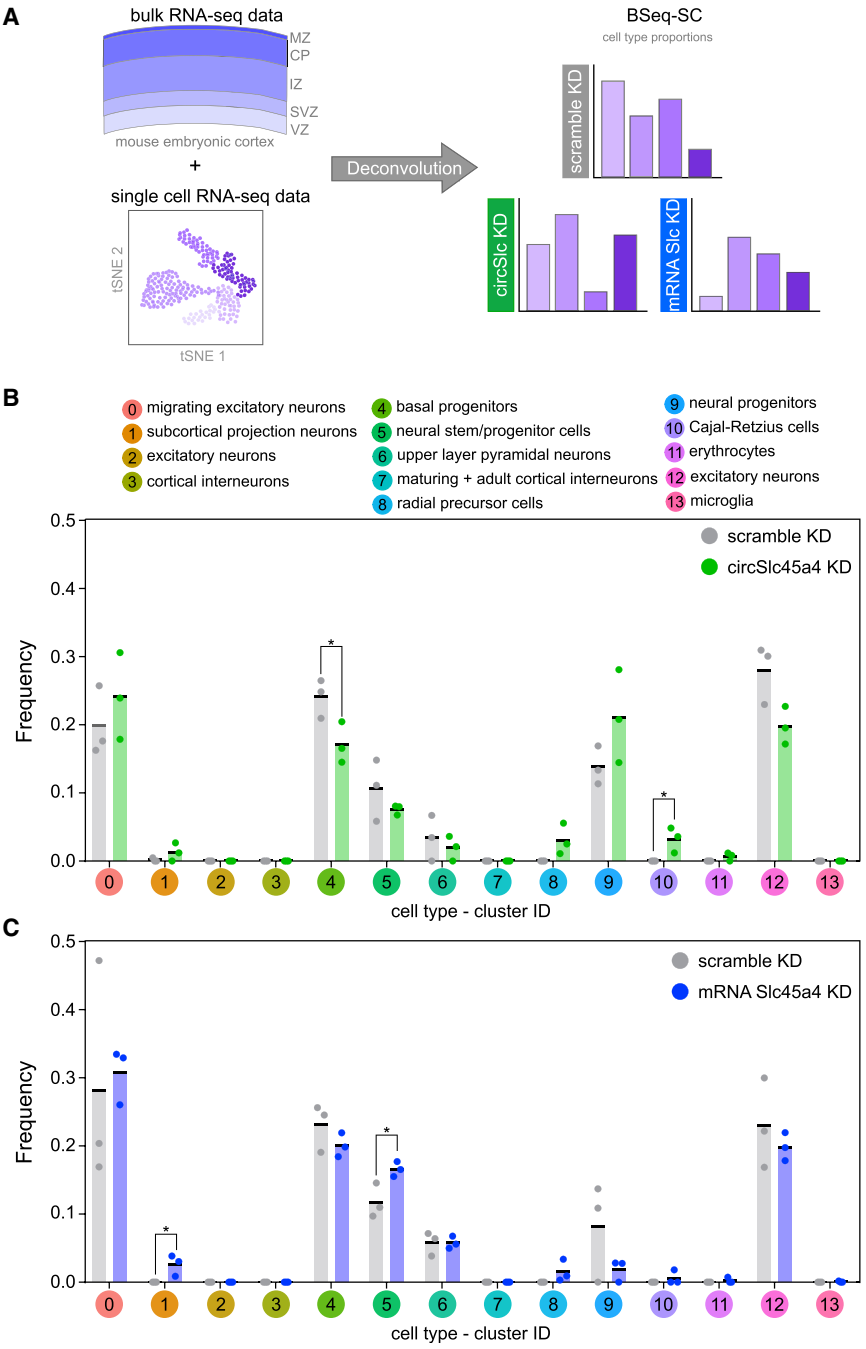

Figure 5. Informing the Bulk RNA-Seq Data with a Single-Cell Dataset Confirms the Depletion of BPs and Reveals an Increase in Cajal-Retzius Cells

(A) General workflow of Bseq-SC. Single-cell RNA-seq data are used to decouple changes introduced by the KD from variations in cell populations.

(B) Shifts in cell population between scramble KD and circ*Slc45a4* KD. Cluster 4 (BPs) and cluster 10 (Cajal-Retzius cells) are significantly altered; t test; $^{*}p < 0.05$.

(C) Shifts in cell population between scramble KD and mRNA *Slc45a4* KD. Cluster 1 (subcortical projection NEUs) and cluster 5 (neural stem and/or progenitor cells) are significantly altered; t test; $^{*}p < 0.05$.

See also Figure S5.

were used and only effects observed for each of these siRNAs were considered;, (2) siSPOTR (Boudreau et al., 2013) was used to minimize the chance of hitting unintended targets with potential miRNA seed sequences included in the siRNA or shRNA; (3) BLAST (Altschul et al., 1990) analysis of the siRNA and shRNA sequences was used to ensure that no other RNAs will be targeted by the siRNA; and (4) ensure isoform-specific KD in a cell line model (mouse P19) to minimize the number of animals that were needed to be sacrificed for this study.

circ*SLC45A4* and mRNA *SLC45A4* originate from the same genetic locus. Hence, they are identical in their sequence, except for the head-to-tail splice junction that is specific to the circRNA. Therefore, ensuring that the effects described for perturbation of the circRNA are indeed caused by the circRNA and not through secondary effects on the mRNA is of great importance. To do so, we designed all siRNAs against the circRNA to be specific to the httj. Therefore, the circRNA-specific siRNAs are not able to target the mRNA, as the siRNAs and/or shRNAs would only overlap with the mRNA sequence by 12 nt. In addition, we show that the mRNA levels are unperturbed in SH-SY5Y cells after KD of the circRNA with 2 of the 3 siRNAs used. The other siRNA that was designed against the circRNA causes a downregulation of the mRNA by 26%. In the mouse cortex, the mRNA levels are reduced by 25% after KD of the circular RNA. This downregulation may be caused by distorted cell-type ratios, as we have validated the isoform specificity of the used shRNAs in a mouse cell line. We do not observe the same changes in the shRNA KD targeting the mRNA as for the circRNA KD. While the mRNA KD reduces the number of cells in the CP, the circRNA KD additionally reduced the number of cells in the SVZ significantly. Also, the effect on BPs, which was validated by quantification of the electroporation experiments but also by RNA-seq in conjunction with independent single-cell RNA-seq data, is observed only after circRNA KD.

Ideally, we would have confirmed the specificity of all of these observed effects with a rescue experiment in which a non-targetable circ*SLC45A4* would have been overexpressed as the endogenous circular RNA is downregulated by the siRNAs

or shRNAs. However, overexpression of circRNAs is not trivial, as the biogenesis of them is not fully understood. Overexpression from plasmid constructs, with or without surrounding introns, yielded an unintended linear by-product. This unintended linear by-product was in vast excess over the intended circRNA.

How, therefore, can the phenotypes observed in SH-SY5Y cells, spontaneous induction of neurogenesis, and, in mouse cortex, depletion of the BP pool, be reconciled? In both cases, we observe the depletion of a neuronal progenitor pool: SH-SY5Y cells are already mainly neuroblasts that are spontaneously differentiating toward a neuronal phenotype after the depletion of circ*SLC45A4*. In the mouse cortex, we have several lines of evidence that show the depletion of the BP pool already in the VZ. BPs can be generated from APs or from BPs themselves. BPs also undergo symmetric, neurogenic divisions and thereby generate NEU in the developing cortex (Taverna et al., 2014). In addition to the depletion of the BP pool, we observed a slight but significant increase in APs; the number of NEUs, however, was not affected. It would have been interesting to study any long-term effects that the depletion of circ*Slc45a4* may have on cortical development in mice. However, electroporation and RNAi are transient manipulations. To causally connect effects observed in postnatal mouse brain with a transient manipulation conducted in embryos is challenging. A knockout mouse may provide additional long-term insights, as it may allow a permanent perturbation of expression levels, but as long as circRNA biogenesis is not sufficiently understood, one cannot modulate the expression levels of circRNAs that overlap with an mRNA, as a deletion of the locus will result in the deletion of both RNA isoforms.

What causes this distortion in the AP:BP pool ratio? Here, the increased number of Cajal-Retzius cells that was determined from the combined analysis of bulk RNA-seq and single-cell RNA-seq data seems intriguing. Pre-existing single-cell RNA-seq data of embryonic mouse cortex were used (Yuzwa et al., 2017) to identify marker genes for the present cell types. In using this pre-existing data, we are relying on the assumption that the cellular architecture of the embryonic mouse cortex is highly reproducible and stable at the investigated developmental time point. In addition, this approach saves considerable resources (e.g., mice, sequencing costs). From this analysis, we predicted that circ*Slc45a4* KD would cause a depletion of BPs and an increase in Cajal-Retzius cells. These results were consistently obtained from bioinformatic predictions and *in vivo* data, corroborating the validity of our deconvolution approach. Cajal-Retzius cells are the first type of NEU appearing in the neocortex. Their main function is to secrete reelin, an extracellular matrix glycoprotein that helps to mediate neuronal migration and controls cell-cell interactions in the developing brain (Gupta et al., 2002). Furthermore, it was shown that reelin influences the proliferation of APs by amplifying Notch signaling (Lakomá et al., 2011). Notch2 and Rbpj were among the most strongly and significantly upregulated genes after circ*Slc45a4* KD in the developing mouse cortex. The amplification of Notch signaling through reelin promotes the symmetric proliferative divisions of APs (Lakomá et al., 2011). This could explain the observed increase in the number of APs, while there are fewer BPs.

STAR★METHODS

Detailed methods are provided in the online version of this paper and include the following:

- KEY RESOURCES TABLE
- LEAD CONTACT AND MATERIALS AVAILABILITY
- EXPERIMENTAL MODEL AND SUBJECT DETAILS
  - Animals
  - Maintenance and Differentiation of SH-SY5Y cells
  - Maintenance and differentiation of NTERA-2 cells
  - Maintenance of P19 cells
- METHOD DETAILS
  - RNA sequencing and data analysis
  - Conservation
  - Reanalysis of single-cell data and marker gene determination
  - Knockdowns in cell lines
  - RNA extraction
  - Neurite length quantification
  - Stellaris single molecule FISH
  - Basescope staining of cortical sections
  - Cell fractionation
  - Immunofluorescence staining of cell lines
  - Reverse transcription and qPCR
  - In utero electroporation & FACS of GFP+ cells
  - Immunofluorescence staining of cortical slices & quantification
  - Western Blot
- QUANTIFICATION AND STATISTICAL ANALYSIS
- DATA AND CODE AVAILABILITY

SUPPLEMENTAL INFORMATION

Supplemental Information can be found online at https://doi.org/10.1016/j.celrep.2020.01.083.

ACKNOWLEDGMENTS

We thank Agnieszka Rybak-Wolf and Martina Dori for initial discussions of the project; Salah Ayoub, Anastasiya Boltengagen, Gwendolin Matz, and Luisa Schreyer for technical support; and the entire Rajewsky lab for discussions, helpful comments, and sharing code, especially David Koppstein for thorough discussion of the manuscript. C.S. is grateful to B. Suenkel (MDC Berlin, Sommer lab) for manifold support and discussions. C.S. acknowledges funding from the Boehringer Ingelheim Fonds (BIF), S.M. and F.C. were supported by the CRTD, the School of Medicine of TU Dresden (DFG CA 893/9-1), and D.C. was funded by the Dresden International Graduate School for Biomedicine and Bioengineering (DIGS-BB), granted by the Deutsche Forschungsgemeinschaft (DFG) in the context of the Excellence Initiative (project GSC 97).

AUTHOR CONTRIBUTIONS

C.S. and N.R. conceived the project. C.S. designed and conducted all of the experiments and analysis, except for the *in utero* electroporation and quantification on cortical mouse slices, which were done by D.C. and S.M. in the laboratory of F.C. C.S., D.C., F.C., and N.R. discussed and interpreted the results. C.S. and N.R. wrote the manuscript with input from D.C. and F.C. N.R. supervised the project.

DECLARATION OF INTERESTS

The authors declare no competing interests.

Received: February 22, 2019
Revised: November 19, 2019
Accepted: January 23, 2020
Published: February 18, 2020

REFERENCES

Altschul, S.F., Gish, W., Miller, W., Myers, E.W., and Lipman, D.J. (1990). Basic local alignment search tool. J. Mol. Biol. *215*, 403–410.

Anders, S., Pyl, P.T., and Huber, W. (2015). HTSeq–a Python framework to work with high-throughput sequencing data. Bioinformatics *31*, 166–169.

Angevine, J.B., Jr., and Sidman, R.L. (1961). Autoradiographic study of cell migration during histogenesis of cerebral cortex in the mouse. Nature *192*, 766–768.

Aprea, J., and Calegari, F. (2015). Long non-coding RNAs in corticogenesis: deciphering the non-coding code of the brain. EMBO J. *34*, 2865–2884.

Aprea, J., Prenninger, S., Dori, M., Ghosh, T., Monasor, L.S., Wessendorf, E., Zocher, S., Massalini, S., Alexopoulou, D., Lesche, M., et al. (2013). Transcriptome sequencing during mouse brain development identifies long non-coding RNAs functionally involved in neurogenic commitment. EMBO J. *32*, 3145–3160.

Artegiani, B., Lange, C., and Calegari, F. (2012). Expansion of embryonic and adult neural stem cells by in utero electroporation or viral stereotaxic injection. J. Vis. Exp. (*68*), 4093.

Ashwal-Fluss, R., Meyer, M., Pamudurti, N.R., Ivanov, A., Bartok, O., Hanan, M., Evantal, N., Memczak, S., Rajewsky, N., and Kadener, S. (2014). circRNA biogenesis competes with pre-mRNA splicing. Mol. Cell *56*, 55–66.

Baron, M., Veres, A., Wolock, S.L., Faust, A.L., Gaujoux, R., Vetere, A., Ryu, J.H., Wagner, B.K., Shen-Orr, S.S., Klein, A.M., et al. (2016). A Single-Cell Transcriptomic Map of the Human and Mouse Pancreas Reveals Inter- and Intra-cell Population Structure. Cell Syst. *3*, 346–360.e4.

Boudreau, R.L., Spengler, R.M., Hylock, R.H., Kusenda, B.J., Davis, H.A., Eichmann, D.A., and Davidson, B.L. (2013). siSPOTR: a tool for designing highly specific and potent siRNAs for human and mouse. Nucleic Acids Res. *41*, e9.

Butler, A., Hoffman, P., Smibert, P., Papalexi, E., and Satija, R. (2018). Integrating single-cell transcriptomic data across different conditions, technologies, and species. Nat. Biotechnol. *36*, 411–420.

Chomczynski, P., and Sacchi, N. (1987). Single-step method of RNA isolation by acid guanidinium thiocyanate-phenol-chloroform extraction. Anal. Biochem. *162*, 156–159.

Dobin, A., Davis, C.A., Schlesinger, F., Drenkow, J., Zaleski, C., Jha, S., Batut, P., Chaisson, M., and Gingeras, T.R. (2013). STAR: ultrafast universal RNA-seq aligner. Bioinformatics *29*, 15–21.

Dori, M., Haj Abdullah Alieh, L., Cavalli, D., Massalini, S., Lesche, M., Dahl, A., and Calegari, F. (2019). Sequence and expression levels of circular RNAs in progenitor cell types during mouse corticogenesis. Life Sci. Alliance *2*, e201900354.

Du, W.W., Yang, W., Liu, E., Yang, Z., Dhaliwal, P., and Yang, B.B. (2016). Foxo3 circular RNA retards cell cycle progression via forming ternary complexes with p21 and CDK2. Nucleic Acids Res. *44*, 2846–2858.

Elbashir, S.M., Harborth, J., Lendeckel, W., Yalcin, A., Weber, K., and Tuschl, T. (2001). Duplexes of 21-nucleotide RNAs mediate RNA interference in cultured mammalian cells. Nature *411*, 494–498.

ENCODE Project Consortium (2012). An integrated encyclopedia of DNA elements in the human genome. Nature *489*, 57–74.

Englund, C., Fink, A., Lau, C., Pham, D., Daza, R.A.M., Bulfone, A., Kowalczyk, T., and Hevner, R.F. (2005). Pax6, Tbr2, and Tbr1 are expressed sequentially by radial glia, intermediate progenitor cells, and postmitotic neurons in developing neocortex. J. Neurosci. *25*, 247–251.

Finlay, B.L., and Darlington, R.B. (1995). Linked regularities in the development and evolution of mammalian brains. Science *268*, 1578–1584.

Florio, M., and Huttner, W.B. (2014). Neural progenitors, neurogenesis and the evolution of the neocortex. Development *141*, 2182–2194.

Glažar, P., Papavasileiou, P., and Rajewsky, N. (2014). circBase: a database for circular RNAs. RNA *11*, 1666–1670.

Götz, M., and Huttner, W.B. (2005). The cell biology of neurogenesis. Nat. Rev. Mol. Cell Biol. *6*, 777–788.

Gupta, A., Tsai, L.-H., and Wynshaw-Boris, A. (2002). Life is a journey: a genetic look at neocortical development. Nat. Rev. Genet. *3*, 342–355.

Hansen, T.B., Jensen, T.I., Clausen, B.H., Bramsen, J.B., Finsen, B., Damgaard, C.K., and Kjems, J. (2013). Natural RNA circles function as efficient microRNA sponges. Nature *495*, 384–388.

Hinrichs, A.S., Karolchik, D., Baertsch, R., Barber, G.P., Bejerano, G., Clawson, H., Diekhans, M., Furey, T.S., Harte, R.A., Hsu, F., et al. (2006). The UCSC Genome Browser Database: update 2006. Nucleic Acids Res. *34*, D590–D598.

Ivanov, A., Memczak, S., Wyler, E., Torti, F., Porath, H.T., Orejuela, M.R., Piechotta, M., Levanon, E.Y., Landthaler, M., Dieterich, C., and Rajewsky, N. (2015). Analysis of intron sequences reveals hallmarks of circular RNA biogenesis in animals. Cell Rep. *10*, 170–177.

Kleaveland, B., Shi, C.Y., Stefano, J., and Bartel, D.P. (2018). A network of noncoding regulatory RNAs acts in the mammalian brain. Cell *174*, 350–362.e17.

Komuro, H., and Rakic, P. (1998). Distinct modes of neuronal migration in different domains of developing cerebellar cortex. J. Neurosci. *18*, 1478–1490.

Kovalevich, J., and Langford, D. (2013). Considerations for the use of SH-SY5Y neuroblastoma cells in neurobiology. Methods Mol. Biol. *1078*, 9–21.

Kriegstein, A.R., and Noctor, S.C. (2004). Patterns of neuronal migration in the embryonic cortex. Trends Neurosci. *27*, 392–399.

Laemmli, U.K. (1970). Cleavage of structural proteins during the assembly of the head of bacteriophage T4. Nature *227*, 680–685.

Lakomá, J., Garcia-Alonso, L., and Luque, J.M. (2011). Reelin sets the pace of neocortical neurogenesis. Development *138*, 5223–5234.

Lawrence, M., Huber, W., Pagès, H., Aboyoun, P., Carlson, M., Gentleman, R., Morgan, M.T., and Carey, V.J. (2013). Software for computing and annotating genomic ranges. PLoS Comput. Biol. *9*, e1003118.

Lee, V.M., and Andrews, P.W. (1986). Differentiation of NTERA-2 clonal human embryonal carcinoma cells into neurons involves the induction of all three neurofilament proteins. J. Neurosci. *6*, 514–521.

Legnini, I., Di Timoteo, G., Rossi, F., Morlando, M., Briganti, F., Sthandier, O., Fatica, A., Santini, T., Andronache, A., Wade, M., et al. (2017). Circ-ZNF609 Is a Circular RNA that Can Be Translated and Functions in Myogenesis. Mol. Cell *66*, 22–37.e9.

Liao, Y., Smyth, G.K., and Shi, W. (2013). The Subread aligner: fast, accurate and scalable read mapping by seed-and-vote. Nucleic Acids Res. *41*, e108.

Love, M.I., Huber, W., and Anders, S. (2014). Moderated estimation of fold change and dispersion for RNA-seq data with DESeq2. Genome Biol. *15*, 550.

Maass, P.G., Glažar, P., Memczak, S., Dittmar, G., Hollfinger, I., Schreyer, L., Sauer, A.V., Toka, O., Aiuti, A., Luft, F.C., and Rajewsky, N. (2017). A map of human circular RNAs in clinically relevant tissues. J. Mol. Med. (Berl.) *95*, 1179–1189.

McBurney, M.W., and Rogers, B.J. (1982). Isolation of male embryonal carcinoma cells and their chromosome replication patterns. Dev. Biol. *89*, 503–508.

Memczak, S., Jens, M., Elefsinioti, A., Torti, F., Krueger, J., Rybak, A., Maier, L., Mackowiak, S.D., Gregersen, L.H., Munschauer, M., et al. (2013). Circular RNAs are a large class of animal RNAs with regulatory potency. Nature *495*, 333–338.

Mihalas, A.B., Elsen, G.E., Bedogni, F., Daza, R.A.M., Ramos-Laguna, K.A., Arnold, S.J., and Hevner, R.F. (2016). Intermediate progenitor cohorts differentially generate cortical layers and require tbr2 for timely acquisition of neuronal subtype identity. Cell Rep. *16*, 92–105.

Mora-Bermúdez, F., García, M.T., and Huttner, W.B. (2013). Stem cells: neural stem cells in cerebral cortex development. In Neuroscience in the 21st Century, D.W. Pfaff, ed. (Springer New York), pp. 137–159.

Noctor, S.C., Martinez-Cerdeño, V., and Kriegstein, A.R. (2007). Neural stem and progenitor cells in cortical development. Novartis Found. Symp. *288*, 59–73, discussion 73–78, 96–98.

Påhlman, S., Ruusala, A.I., Abrahamsson, L., Mattsson, M.E., and Esscher, T. (1984). Retinoic acid-induced differentiation of cultured human neuroblastoma cells: a comparison with phorbolester-induced differentiation. Cell Differ. *14*, 135–144.

Pamudurti, N.R., Bartok, O., Jens, M., Ashwal-Fluss, R., Stottmeister, C., Ruhe, L., Hanan, M., Wyler, E., Perez-Hernandez, D., Ramberger, E., et al. (2017). Translation of CircRNAs. Mol. Cell *66*, 9–21.e7.

Paridaen, J.T.M.L., and Huttner, W.B. (2014). Neurogenesis during development of the vertebrate central nervous system. EMBO Rep. *15*, 351–364.

Pfaffl, M.W. (2001). A new mathematical model for relative quantification in real-time RT-PCR. Nucleic Acids Res. *29*, e45.

Piwecka, M., Glažar, P., Hernandez-Miranda, L.R., Memczak, S., Wolf, S.A., Rybak-Wolf, A., Filipchyk, A., Klironomos, F., Cerda Jara, C.A., Fenske, P., et al. (2017). Loss of a mammalian circular RNA locus causes miRNA deregulation and affects brain function. Science *357*, eaam8526.

Pleasure, S.J., and Lee, V.M. (1993). NTera 2 cells: a human cell line which displays characteristics expected of a human committed neuronal progenitor cell. J. Neurosci. Res. *35*, 585–602.

Podrygajlo, G., Tegenge, M.A., Gierse, A., Paquet-Durand, F., Tan, S., Bicker, G., and Stern, M. (2009). Cellular phenotypes of human model neurons (NT2) after differentiation in aggregate culture. Cell Tissue Res. *336*, 439–452.

Pollard, K.S., Hubisz, M.J., Rosenbloom, K.R., and Siepel, A. (2010). Detection of nonneutral substitution rates on mammalian phylogenies. Genome Res. *20*, 110–121.

Raj, A., and Tyagi, S. (2010). Detection of individual endogenous RNA transcripts in situ using multiple singly labeled probes. Methods Enzymol. *472*, 365–386.

Ritchie, M.E., Phipson, B., Wu, D., Hu, Y., Law, C.W., Shi, W., and Smyth, G.K. (2015). limma powers differential expression analyses for RNA-sequencing and microarray studies. Nucleic Acids Res. *43*, e47.

Ross, R.A., Spengler, B.A., and Biedler, J.L. (1983). Coordinate morphological and biochemical interconversion of human neuroblastoma cells. J. Natl. Cancer Inst. *71*, 741–747.

Rybak-Wolf, A., Stottmeister, C., Glažar, P., Jens, M., Pino, N., Giusti, S., Hanan, M., Behm, M., Bartok, O., Ashwal-Fluss, R., et al. (2015). Circular RNAs in the mammalian brain are highly abundant, conserved, and dynamically expressed. Mol. Cell *58*, 870–885.

Salzman, J., Gawad, C., Wang, P.L., Lacayo, N., and Brown, P.O. (2012). Circular RNAs are the predominant transcript isoform from hundreds of human genes in diverse cell types. PLoS One *7*, e30733.

Salzman, J., Chen, R.E., Olsen, M.N., Wang, P.L., and Brown, P.O. (2013). Cell-type specific features of circular RNA expression. PLoS Genet. *9*, e1003777.

Schindelin, J., Arganda-Carreras, I., Frise, E., Kaynig, V., Longair, M., Pietzsch, T., Preibisch, S., Rueden, C., Saalfeld, S., Schmid, B., et al. (2012). Fiji: an open-source platform for biological-image analysis. Nat. Methods *9*, 676–682.

Stagni, F., Giacomini, A., Guidi, S., Ciani, E., and Bartesaghi, R. (2015). Timing of therapies for Down syndrome: the sooner, the better. Front. Behav. Neurosci. *9*, 265.

Starke, S., Jost, I., Rossbach, O., Schneider, T., Schreiner, S., Hung, L.-H., and Bindereif, A. (2015). Exon circularization requires canonical splice signals. Cell Rep. *10*, 103–111.

Sun, T., and Hevner, R.F. (2014). Growth and folding of the mammalian cerebral cortex: from molecules to malformations. Nat. Rev. Neurosci. *15*, 217–232.

Taverna, E., Götz, M., and Huttner, W.B. (2014). The cell biology of neurogenesis: toward an understanding of the development and evolution of the neocortex. Annu. Rev. Cell Dev. Biol. *30*, 465–502.

Vitavska, O., and Wieczorek, H. (2017). Putative role of an SLC45 H(+)/sugar cotransporter in mammalian spermatozoa. Pflugers Arch. *469*, 1433–1442.

Wang, P.L., Bao, Y., Yee, M.-C., Barrett, S.P., Hogan, G.J., Olsen, M.N., Dinneny, J.R., Brown, P.O., and Salzman, J. (2014). Circular RNA is expressed across the eukaryotic tree of life. PLoS One *9*, e90859.

Wilsch-Bräuninger, M., Florio, M., and Huttner, W.B. (2016). Neocortex expansion in development and evolution - from cell biology to single genes. Curr. Opin. Neurobiol. *39*, 122–132.

You, X., Vlatkovic, I., Babic, A., Will, T., Epstein, I., Tushev, G., Akbalik, G., Wang, M., Glock, C., Quedenau, C., et al. (2015). Neural circular RNAs are derived from synaptic genes and regulated by development and plasticity. Nat. Neurosci. *18*, 603–610.

Yuzwa, S.A., Borrett, M.J., Innes, B.T., Voronova, A., Ketela, T., Kaplan, D.R., Bader, G.D., and Miller, F.D. (2017). Developmental Emergence of Adult Neural Stem Cells as Revealed by Single-Cell Transcriptional Profiling. Cell Rep. *21*, 3970–3986.

Zhang, X.-O., Wang, H.-B., Zhang, Y., Lu, X., Chen, L.-L., and Yang, L. (2014). Complementary sequence-mediated exon circularization. Cell *159*, 134–147.

STAR★METHODS

KEY RESOURCES TABLE

REAGENT or RESOURCE	SOURCE	IDENTIFIER
Antibodies		
anti-TUBB3 (IF)	BioLegend	801213; RRID:AB_2728521
anti-GFAP	Merck/Millipore	AB5804; RRID:AB_2109645
anti-GFP	Rockland	600-101-215; RRID:AB_218182
anti-Tbr2	abcam	ab183991; RRID:AB_2721040
anti-Pax6	Covance	PRB-278P; RRID:AB_291612
anti-Ctip2	abcam	ab6326; RRID:AB_305426
anti-Reelin	Merck/Millipore	MAB5364; RRID:AB_2179313
anti-TUBB3 (WB)	Sigma-Aldrich	T2200-200UL; RRID:AB_262133
anti-GAPDH	Sigma-Aldrich	G8795-200UL; RRID:AB_1078991
Bacterial and Virus Strains		
DH5 alpha	Zymo Research	T3009
Chemicals, Peptides, and Recombinant Proteins		
all-trans retinoic acid	Sigma-Aldrich	R2625-100MG
AraC	Sigma-Aldrich	C6645
Lipofectamine RNAiMax	Thermo Fisher Scientific	13778150
Lipofectamine 3000	Thermo Fisher Scientific	L3000015
Critical Commercial Assays		
BaseScope Reagent Kit-RED	ACDBio	322900
BaseScope Custom Probes	ACDBio	700001
BaseScope Control Probe Pack	ACDBio	322975
Deposited Data		
SH-SY5Y circSLC45A4 KD and control data	GEO	GSE124001
Embryonic mouse cortex circSlc45a4 KD, mRNA Slc45a4 KD and scramble KD	GEO	GSE124000
Experimental Models: Cell Lines		
SH-SY5Y	ATCC	CRL-2266
NTERA-2	ATCC	CRL-1973
P19	ATCC	CRL-1825
Experimental Models: Organisms/Strains		
C57BL/6J	The Jackson Laboratory	C57BL/6J
Oligonucleotides		
please refer to Table S3	N/A	N/A
Software and Algorithms		
bcl2fastq	Illumina	N/A
STAR 2.4.1d/2.4.2a	Dobin et al., 2013	N/A
HTseq	Anders et al., 2015	N/A
DESeq2	Love et al., 2014	N/A
limma	Ritchie et al., 2015	N/A
Seurat	Butler et al., 2018	N/A
Bseq-SC	Baron et al., 2016	N/A
GenomicRanges	Lawrence et al., 2013	N/A
Rsubread	Liao et al., 2013	N/A

LEAD CONTACT AND MATERIALS AVAILABILITY

Further information and requests for resources and reagents should be directed to and will be fulfilled by the Lead Contact, Nikolaus Rajewsky (rajewsky@mdc-berlin.de). Plasmids generated (shRNA knockdown of circ*Slc45a4* in mouse) in this study can be obtained from the Rajewsky lab.

EXPERIMENTAL MODEL AND SUBJECT DETAILS

Animals

Plugged C57BL/6J females were purchased from Janvier Labs and housed in the Biomedical Services facility of the MPI-CBG under standard conditions: 12-hour light-dark cycle, 22 ± 2°C temperature, 55 ± 10% humidity, food and water supplied ab libitum. All experimental procedures were performed according to local regulations and all animal experiments were approved by local authorities (Landesdirektion Sachsen; 24D-9168.11-1/41, 2008-16, 2011-11, TVV 39/2015, 13/2016 TVV and 16-2018).

Maintenance and Differentiation of SH-SY5Y cells

SH-SY5Y cells were obtained from ATCC (CRL-2266, female). SH-SY5Y cells were differentiated as previously described (Ross et al., 1983). In brief, cells were grown in DMEM/F12 (GIBCO) with 10% FBS and 1x GlutaMax (GIBCO). For differentiation cells were plated at a density of $1 \cdot 10^5$ cells/cm^2 and induced by addition of differentiation medium (Neurobasal medium, 1x GlutaMax, 1x B27, 10 μM ATRA) and harvested four or eight days later. At day four post-induction 5 μM AraC were added to prevent overgrowth of the culture with mitotic cells. The medium was exchanged every second day.

Maintenance and differentiation of NTERA-2 cells

NTERA-2 cells were obtained from ATCC (CRL-1973, male). NTERA-2 cells were differentiated as previously described (Lee and Andrews, 1986; Pleasure and Lee, 1993; Podrygajlo et al., 2009). In brief, 1x10^6 cells/cm^2 were plated in bacteriological grade dishes in DMEM/F12 (GIBCO), 10% FBS and 1x GlutaMax (GIBCO). After 2 days 10 μM ATRA was added and medium was renewed every two days until day 8. Embryoid bodies were then plated on a cell culture grade dish (same size as initial bacteriological dish) and grown as monolayer. At day 14 cells were trypsinized (5 min, room temperature, 0.05% Trypsin/EDTA) and replated on a larger dish. At day 16 cells were trypsinized again and replated on a smaller dish while the media was additionally supplemented with 1 μm AraC. Finally, at day 23 cells were replated on PLL-coated dishes at a density of 4x10^5 cells/cm^2 as neuronal culture.

Maintenance of P19 cells

P19 cells were obtained from ATCC (CRL-1825, male). P19 cells (McBurney and Rogers, 1982) were maintained in alpha-MEM with 2.5% FBS and 1x GlutaMax (GIBCO).

METHOD DETAILS

RNA sequencing and data analysis

polyA+ libraries were prepared from RNA with Illumina TruSeq RNA Library Prep kit v2 (SH-SY5Y) or Illumina TruSeq Stranded mRNA LT (mouse cortex GFP+ cells) and sequenced on a Illumina NextSeq 500 with 1x150 bp. Sequencing data was converted to fastq and demultiplexed using *bcl2fastq* and mapped to hg38 with STAR 2.4.1d or to mm10 with STAR 2.4.2a (Dobin et al., 2013). Uniquely aligned reads were intersected with GENCODE v23 gene models (human) or GENCODE vM16 (mouse) and counted with HTseq (Anders et al., 2015) (human) or with GenomicRanges (Lawrence et al., 2013) and Rsubread (Liao et al., 2013).

The circRNA-to-mRNA ratio was calculated as previously described (Rybak-Wolf et al., 2015). In brief, the reads spanning the head-to-tail junction are taken as measure for circRNA expression. For mRNA expression the maximum number of reads spanning one of either splice junctions adjacent to the head-to-tail splice junction is used. From this a ratio is calculated.

Differential expression changes were determined with DESeq2 (Love et al., 2014). The principal component analysis was done with *plotPCA* on regularized log transformed read counts.

For GO term analysis, up- and downregulated genes were selected according to an expression cut-off (> 50 counts in scramble KD) and a significance cut-off (human: adjusted p value < 0.05; mouse: adjusted p value < 0.001). *goana* from the limma package (Ritchie et al., 2015) was used to test for overrepresentation of specific terms, given p values are calculated with a Fisher's exact test and adjusted with the Benjamini-Hochberg method.

Conservation

PhyloP scores (Pollard et al., 2010) from the multiple alignment of 100 vertebrates were retrieved for hg19 using the UCSC table browser (Hinrichs et al., 2006). The mean was calculated for the following genomic regions (hg19): *SLC45A4* exon 1 (circRNA exon) chr8:142,264,087-142,264,728; *SLC45A4* exon 2 chr8:142,231,675-142,231,864; *SLC45A4* exon 3 chr8:142,229,747-142,229,929; *SLC45A4* exon 8 (CDS and 3′-UTR) chr8:142,220,870-142,221,800; *SLC45A1* exon 1 chr1:8,377,887-8,378,248; *SLC45A2* exon 1 chr5:33,984,302-33,984,835; *SLC45A3* exon 1 chr1:205,633,612-205,634,014.

Reanalysis of single-cell data and marker gene determination

Single-cell data from mouse cortex E15.5 was taken from Yuzwa et al. (2017) and downloaded from GEO (GSE107122, "GSE107122_E155_Combined_All_Cells_DGE.txt"). Seurat was used for the re-analysis of this dataset (Butler et al., 2018). Only non-mitochondrial genes that were expressed in $\geq$ 3 cells and cells that had $\geq$ 200 or $\leq$ 6000 genes expressed were kept. Data was normalized (*NormalizeData)*, variable genes were identified (*FindVariableGenes),* data was scaled (*ScaleData)* and principal components identified (*RunPCA)* and statistically significant principal components identified (*PCElbowPlot*, 1 to 16 were selected) with standard settings. Next, 14 cell clusters were identified (*FindClusters*, dims.use = 1:16, resolution = 1.0), visualized with non-linear dimensional reduction (tSNE) as implemented in Seurat. Marker genes for these clusters were identified using the build in *FindAllMarkers* function and then individually evaluated for specific expression in the respective clusters. Based on these marker genes, the identity of the clusters was determined by literature research.

Inference of cell type proportion changes from single-cell and RNA-seq data

Marker genes for the different cell populations present in E15.5 mouse cortex were defined by reanalyzing single-cell data (Yuzwa et al., 2017) (GSE107122, "GSE107122_E155_Combined_All_Cells_DGE.txt"). Bseq-SC (Baron et al., 2016) was used to infer the changes in cell type proportions.

Knockdowns in cell lines

RNAi based knockdown of circ*SLC45A4* in SH-SY5Y cells was done according to standard protocols with Lipofectamine RNAiMax (ThermoFisher). Briefly, $2x10^5$ cells/6-well were seeded in a 6-well plate the day before transfection. 25 pmol of siRNA were used to achieve knockdown of the intended target. SH-SY5Y cells were harvested 96 h post-transfection in Trizol.

Plasmids for shRNA knockdown in P19 cells were generated by replacement of the Hygromycin cassette of pSilencer2.1-U6-hygro (Thermo Fisher) with a nuclear-localized GFP, followed by insertion of shRNAs (purchased as synthetic oligonucleotides from Eurofins). The knockdown was conducted according to the manufacturer's protocol (ThermoFisher, Lipofectamine 3000). In brief, $3x10^5$ cells/6-well were seeded the day before transfection. Then, 3 μg of endotoxin-free plasmid were transfected. 96 h post-transfection cells were washed with 1xPBS and harvested in Trizol for RNA extraction.

RNA extraction

RNA was extracted using Trizol (Chomczynski and Sacchi, 1987). Adherent cells were washed once with 1x PBS pH 7.4 and Trizol was directly added. The samples were incubated for 5 min at room temperature to facilitate complete dissociation. Then 200 μL of Chloroform were added, samples were shaken vigorously and immediately centrifuged (15 min, 12 000xg, 4°C). The upper aqueous phase was recovered and contained RNA was precipitated by adding the same volume of isopropanol. Samples were inverted and incubated for at least 10 min at −20°C. To further aid precipitation of samples with low RNA content, 0.5 μl Glycogen (Glycoblue) were added and samples were incubated for up to 16 h at −20°C before pelleting of the RNA and to further aid precipitation of RNA. Pelleting of the RNA was achieved by centrifugation (20 min, 16 000xg, 4°C). The supernatant was discarded and the RNA pellet was washed twice with 80% (v/v) ethanol. The pellet was dried (5 min, room temperature) and resuspended in water. RNA from electroporated cells was extracted using Quick RNA micro prep kit (Zymo research) following the manufacturer's protocol.

Neurite length quantification

Fiji (Schindelin et al., 2012) was used to quantify neurite length on brightfield microscopy images taken at 20x with a Keyence BZ 9000. The freehand linetool was used to trace neurites starting from the cell body to the neurite tip. The measure tool was used to determine the length in μm. 30 cells per condition were counted.

Stellaris single molecule FISH

Stellaris single molecule FISH was done according to the manufacturer's protocols (Biosearch Technologies). For circ*SLC45A4* 28 probes were used and for mRNA *SLC45A4* as well. As a negative control, samples were carried through the protocol without addition of probes (data not shown).

The sequences of all Stellaris probes used can be found in Table S1.

Basescope staining of cortical sections

The BaseScope assay by ACD can be used to detect single splice junctions. The signal strength is increased by using a branched DNA detection system (ACDBio). In brief, embryonic mouse brain was fixed with 4% PFA overnight, cryoprotected with 30% sucrose, also overnight, and then frozen in tissue freezing medium. Then slides were cryosectioned at 10 μm and carried through the BaseScope standard protocol for fixed frozen tissue sections, except that proteinase digest was limited to 10 min at room temperature to avoid over digestion. Probes against circ*Slc45a4* and mRNA *Slc45a4* are splice-junction specific and were custom produced by ACD, the negative control would target the bacterial *DapB*.

Slices were mounted with one drop of Vectashield Hardset Mounting Medium with DAPI and imaged using a Keyence BZ 9000 microscope.

Cell fractionation

For cell fractionation a kit provided by abcam was used (ab109719). RNA was extracted from cytoplasmic, nuclear and mitochondrial fractions with Trizol and analyzed by RT-qPCR. Sufficient fractionation of the cells was monitored by using ACTB and GAPDH as positive control for the cytoplasmic fraction, XIST and NEAT1 for the nuclear fraction and MT-CO2 for the mitochondrial fraction.

Immunofluorescence staining of cell lines

Immunofluorescence staining was done according to standard protocols. In brief, cells were grown on poly-L-lysine (PLL) coated coverslips. Adherent cells were washed three times with PBS, fixed for 20 min with 4% (w/v) paraformaldehyde (PFA) at room temperature and then washed again three times with cold PBS. Cells were permeabilized with PBST (15 min, 4°), again washed twice with PBS and then blocked with blocking solution (1 h, 4°C; 1% (w/v) BSA, 5% (v/v) Normal Goat Serum (ab7481) in PBS). Then the primary antibody was applied, diluted in PBS with 1% (w/v) BSA, and incubate at 4°C overnight. Unbound antibody was washed away by applying cold PBS four times. The secondary antibody (abcam goat anti-mouse 488, ab150113; abcam goat anti-rabbit 647, ab150083) was diluted in blocking solution and applied for 2 h at room temperature (in the dark). Again, unbound antibody was washed away with three PBS washes. To mount the coverslips on microscope slides for imaging, 10 μL Vectashield Mounting Medium with DAPI were used per coverslip. Mounting medium was dried at room temperature for up to 1 h and then coverslips were fixed on the microscope slide with clear nail polish.

Imaging was done with a Zeiss AxioObserver Z1 with an AxioCam MRm.
TUBB3 antibody – BioLegend 801213; 1:1000 (host: mouse)
GFAP antibody – Merck/Millipore AB5804; 1:1000 (host: rabbit)
Negative controls (only secondary antibody) did not show significant stainings (data not shown).

Reverse transcription and qPCR

RNA was reverse transcribed to cDNA using Maxima H Minus Reverse Transcriptase at 100 U per μg RNA. First, up to 1 μg of RNA was mixed with 0.5 mM dNTPs, 0.25 μg random hexamers and filled up to 15 μl with double-distilled water (ddH_2O). This mixture was denatured at 65°C for 5 min in a thermocycler, immediately placed on ice and 100 U/μg RNA of Maxima RT, 4 μl 5x RT Buffer and 0.5 μL Ribolock were added. The cDNA synthesis was carried out with the following program in a thermocycler: 10 min at 25°C, 30 min at 50°C, 5 min at 85°C.

All quantitative real time PCR experiments were conducted on an ABI StepOne Plus machine. Depending on the sample and target gene set, cDNA was diluted 1:10 to 1:100 with ddH_2O and mixed with 2x Maxima SYBR Green/ROX qPCR Master Mix and 3.75 μl of 2.5 μM Primer mix to obtain 15 μL of total reaction volume per well. All measurements were conducted at least in technical triplicates. Relative quantification was achieved by using the comparative $\Delta\Delta C_T$ method (Pfaffl, 2001).

In utero electroporation & FACS of GFP+ cells

Plasmids for IUE were generated by replacement of the Hygromycin cassette of pSilencer2.1-U6-hygro (Thermo Fisher) with a nuclear-localized GFP, followed by insertion of shRNAs (purchased as synthetic oligonucleotides from Eurofins). IUE was performed as previously described (Artegiani et al., 2012). Briefly, C57BL/6J E13.5 pregnant mice were anesthetized with Isoflurane (Baxter) and 2-3 μg of plasmid DNA were injected into the embryo ventricle, followed by the application of 6 electric pulses (30V and 50 ms each at 1 s intervals) through platinum electrodes using a BTX-830 electroporator (Genetronics). Embryo brains were collected at E 15.5 for immunochemistry (whole brain) or FACS-sorting of electroporated cells (GFP+) (lateral cortices). After removal of meninges and ganglionic eminences, cortices were dissociated with papain-based Neural Tissue Dissociation kit (Miltenyi Biotech) and cells were resuspended in 500 μL of ice-cold PBS. DAPI (1:1000) was added for dead cells discrimination and sorting of GFP+ cells was performed by BD FACSAriaTM III (BD Biosciences).

Immunofluorescence staining of cortical slices & quantification

For immunohistochemistry, brains were fixed overnight at 4°C in 4% paraformaldehyde (in 0.1M phosphate buffer), cryoprotected in 30% sucrose and cryosectioned (10 μm thick). For antigen-retrieval cryosections were incubated for 1 h at 70°C (in 0.01 M Citrate Buffer, pH = 6.0), followed by permeabilization for 20 min (in 0.5% Triton X-100), quenching for 30 min (in 0.1 M glycine) and blocking for 1h (10% donkey serum 0.3% Triton X-100) at RT. All primary antibodies were incubated overnight at 4°C (in 3% donkey serum, 0.3% Triton X-100), whereas secondary antibodies for 2 h at RT. Nuclei were counterstained with DAPI. Imaging was performed using an ApoTome fluorescence microscope (Carl Zeiss) and pictures were assembled using Axiovision software (Carl Zeiss). For quantifications, composite pictures were manually analyzed by, first, delimiting the boundaries of the cortical layers (VZ, SVZ, IZ and CP) as identified by Tbr2 staining labeling the SVZ and the characteristic change in nuclear (DAPI) density at the level of the CP. Second, GFP+ electroporated cells were scored in each layer as the subpopulation positive for additional markers (e.g., Tbr2, Pax6 and/or Ctip2) scored on Photoshop CS6 (Adobe) files with sample averages compared by One-way ANOVA. p values < 0.05 were considered significant.

GFP antibody – Rockland 600-1-1-215; 1:400
Tbr2 antibody – Abcam Ab183991; 1:500
Pax6 antibody – Covance PRB-278P, 1:200
Ctip2 antibody – Abcam ab6326, 1:200
Reelin antibody – Merck/Millipore MAB5364, 1:100
Secondary antibodies – Jackson Laboratory; 1:500

Western Blot

Adherent cells were harvested by scraping and centrifugation (500 x g, 5 min, 4°C), washed once with PBS and resuspended with twice the volume of the cell pellet in ice-cold lysis buffer (RIPA buffer: 150 mM NaCl, 1.0% (v/v) NP40, 0.5% (w/v) sodium deoxycholate, 0.1% (w/v) SDS, 50 mM Tris-HCl (pH 8.0), complete mini protease inhibitor). Cells were incubated on ice for 30 min, while the lysate was passed through a 21G needle 6 times. The lysate was cleared by centrifugation (16000 x g, 20 min, 4°C) and the supernatant was kept for SDS-Polyacrylamide gel electrophoresis and western blot analysis.

10 to 20 μg of protein, as determined by BCA assay, were denatured by addition of 5x SDS Loading dye and incubation at 95°C for 5 min. Proteins were then separated by size by SDS-PAGE (Laemmli, 1970). Subsequent transfer of proteins onto a methanol-activated PVDF membrane was achieved by semi-dry blotting in Transfer buffer. The membrane was blocked for 30 min at room temperature with 3% (w/v) skim milk in PBS and incubated with protein specific primary antibody overnight at 4°C, slowly shaking. Unbound primary antibody was washed: 3 times 10 min in PBST, slowly shaking. Secondary antibody was incubated for 2 h at room temperature, slowly shaking, and again unbound secondary antibody was washed away. Detection was achieved by addition of an HRP substrate (Amersham ECL) and the signal was quantified with a Fujifilm LAS4000 and Fiji.

TUBB3 antibody – SIGMA T2200-200UL, 1:2000
GAPDH antibody – SIGMA G8795-200UL, 1:5000

QUANTIFICATION AND STATISTICAL ANALYSIS

All details for quantification and statistical analysis can be found in the figure legends.

Details for GO analysis and in utero electroporations are stated in the Method Details.

DATA AND CODE AVAILABILITY

The datasets generated for this study are available at GEO: SH-SY5Y data: GSE124001 (GEO) and

- mouse cortex data: GSE124000 (GEO).

The code supporting the current study has not been deposited in a public repository because no new methods were developed for this publication, but pre-existing packages have been used. However, the code is available from the Lead Contact or Christin Suenkel (christin.suenkel@mdc-berlin.de).

circ*SLC45A4* refers to hsa_circ_0001829 (circBase ID, Glažar et al., 2014), hg19: chr8:142264087-142264728. Human mRNA *SLC45A4* refers to NM_001286646.1.
circ*Slc45a4* refers to mmu_circ_0005786 (circBase ID), mm9: chr15:73435871-73436506. Mouse mRNA *Slc45a4* refers to NM_001033219.3.

Cell Reports, Volume *30*

Supplemental Information

A Highly Conserved Circular RNA Is Required to Keep Neural Cells in a Progenitor State in the Mammalian Brain

Christin Suenkel, Daniel Cavalli, Simone Massalini, Federico Calegari, and Nikolaus Rajewsky

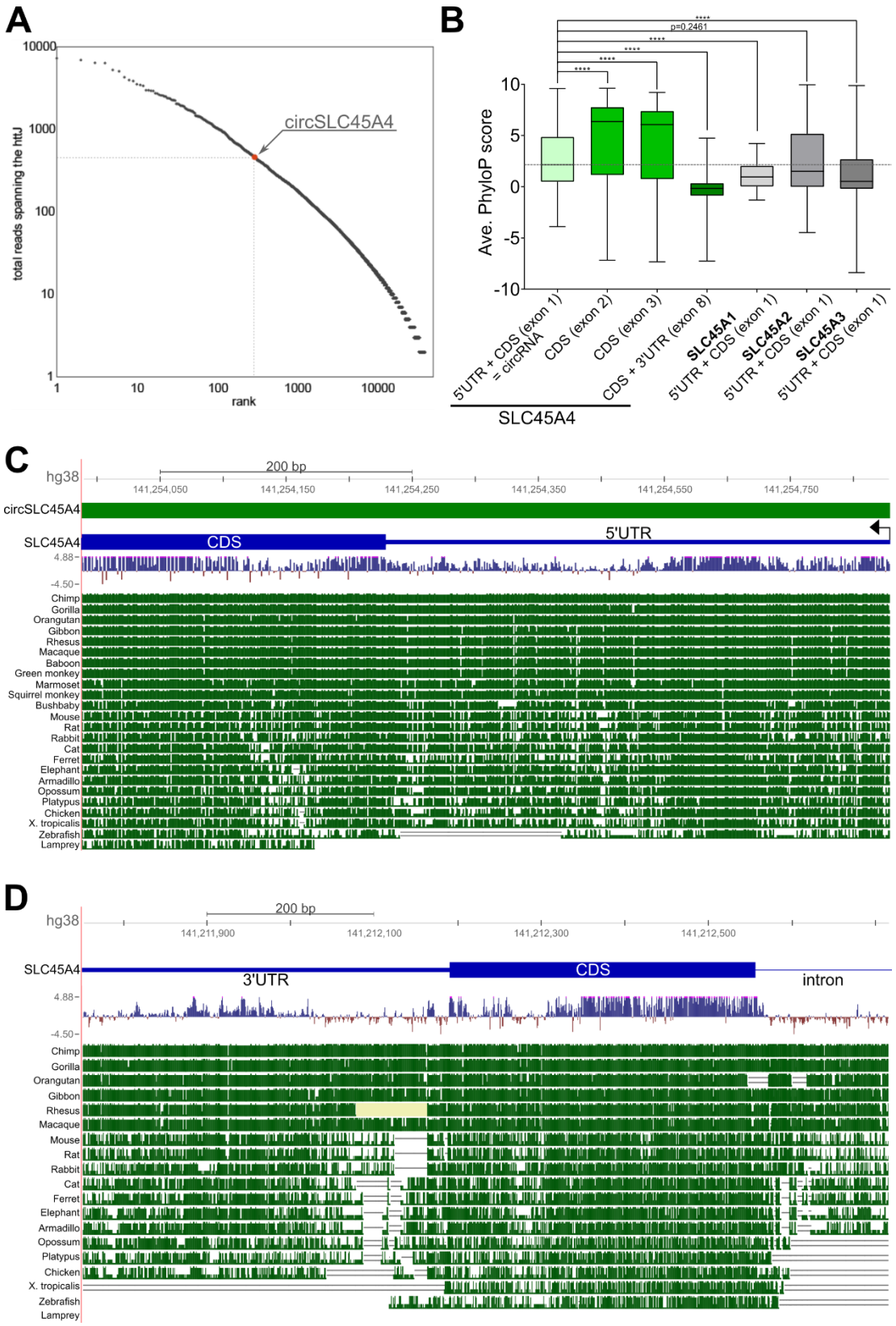

Figure S1: related to Figure 1.
(A) – Expression rank of circSLC45A4 in fetal human cortex, ranked by total reads spanning the head-to-tail splice junction (295th, top 1 %). **(B)** – Average PhyloP scores of multiple alignments of 100 vertebra, SLC45A4 exon1 (641 nt, mean = 2.86), 2 (190 nt, mean = 5.04), 3 (183 nt, mean = 4.52), and 8 (931 nt, mean = -0.25), SLC45A1 exon 1 (103 nt, mean = 1.13), SLC45A2 exon 1 (534 nt, mean = 2.64), SLC45A3 exon 1 (403 nt; mean = 1.73). T-test, p-value < 0.0001 is ****. **(C)** – Genome Browser conservation tracks visualizing the exceptional conservation of circSLC45A4 compared to the 3'UTR and CDS of the same gene, SLC45A4 **(D)**.

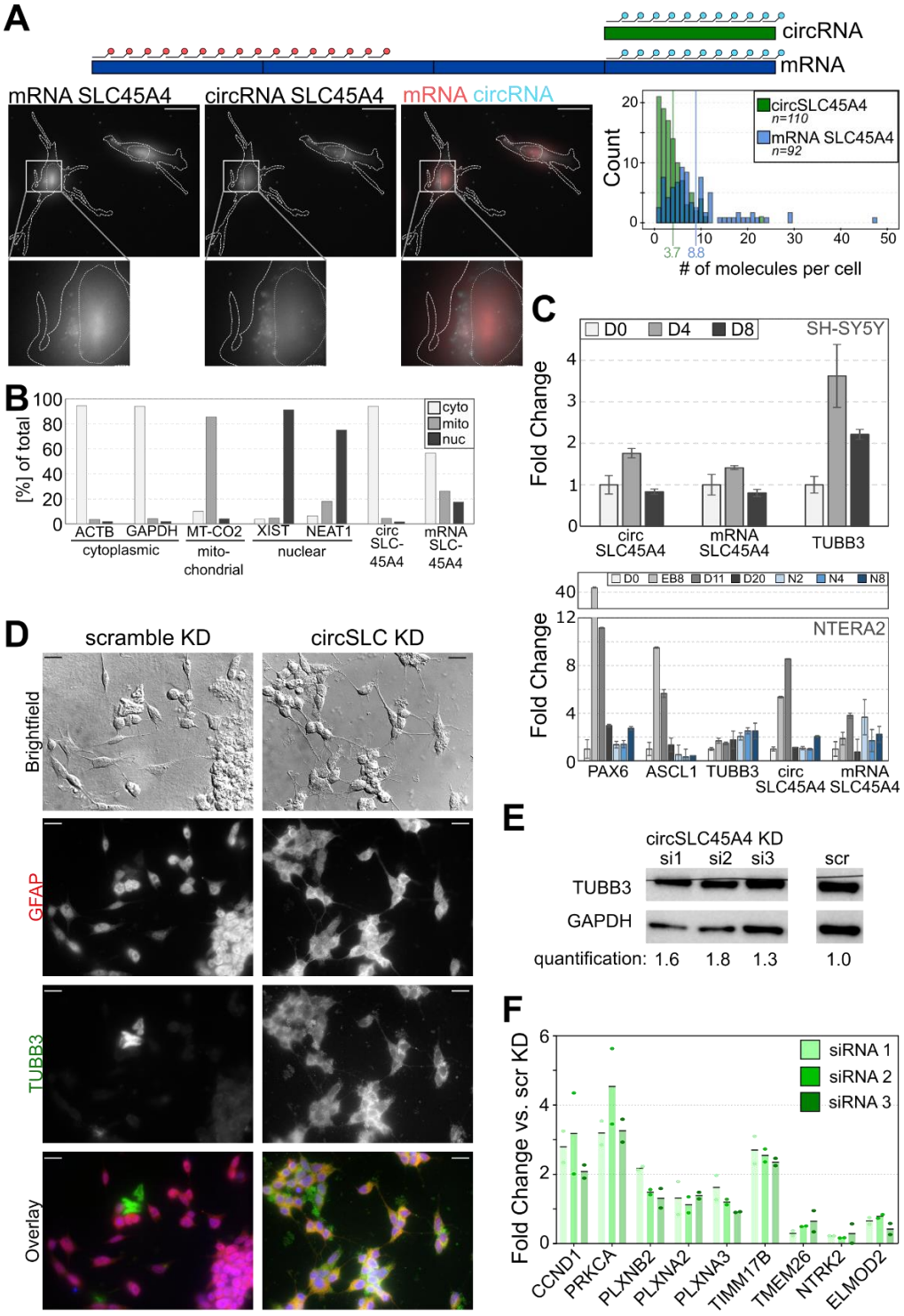

Figure S2: related to Figure 2.

(A) – Single-molecule FISH of circSLC45A4 and mRNA SLC45A4, probe design, representative pictures and quantification in SH-SY5Y. Scale bar corresponds to 10 µm. Cell outlines are marked with dashes, nuclei outlines are marked with dots. Histogram based on n=110 cells for circSLC45A4 and n=92 for mRNA SLC45A4. **(B)** – Fractionation of SH-SY5Y cells shows that circSLC45A4 is largely localized to the cytoplasm, while mRNA SLC45A4 is found mostly in the cytoplasm, but also in mitochondria and in the nucleus. **(C)** – circSLC45A4 expression during SH-SY5Y and NTERA2 differentiation. Expression of important marker genes that highlight the progression of differentiation are shown. Error bars are standard deviation from three technical replicates. **(D)** – Immunofluorescence of SH-SY5Y cells 96 h after knockdown of circSLC45A4, staining for GFAP and TUBB3. Scale bar – 10 µm. **(E)** – Western Blot quantification of TUBB3 protein levels after knockdown of circSLC45A4 with 1 of each of the 3 siRNAs and scramble KD. Fiji was used for quantification. All samples were run on the same membrane, an irrelevant lane was digitally deleted. **(F)** – qPCR validation of selected gene expression changes. Each dot represents one biological replicate.

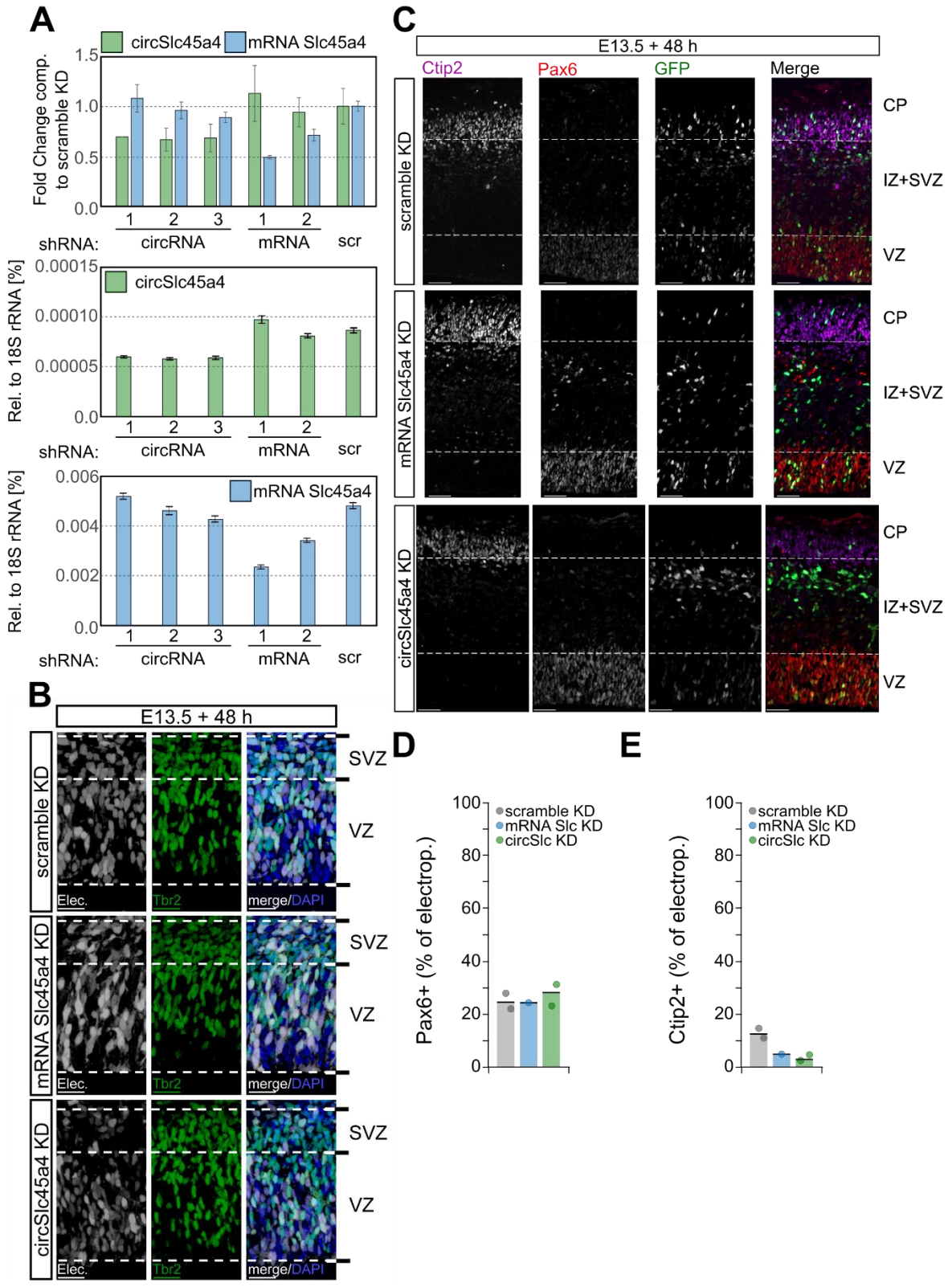

Figure S3: related to Figure 3.
(A) – KD efficiency of the respective shRNAs against circSlc45a4 and mRNA Slc45a4 in mouse P19 cells. Error bars are standard deviation from three technical replicates. **(B)** – Manipulated cells (white – GFP+) in developing cortex at E15.5 for scrambled control KD, mRNA Slc45a4 and circSlc45a4 knockdown. Nuclei are DAPI stained (blue), *co*-staining with Tbr2. Scale bar is 50 µm. **(C)** – Manipulated cells (GFP+), neurons (Ctip2+) and apical progenitors (Pax6+) in developing cortex at E15.5 for scrambled control KD, mRNA Slc45a4 and circSlc45a4 KD. Scale bar is 50 µm. **(D)** – Quantification of electroporated cells that are Pax6+. **(E)** – Quantification of electroporated cells that are Ctip2+.

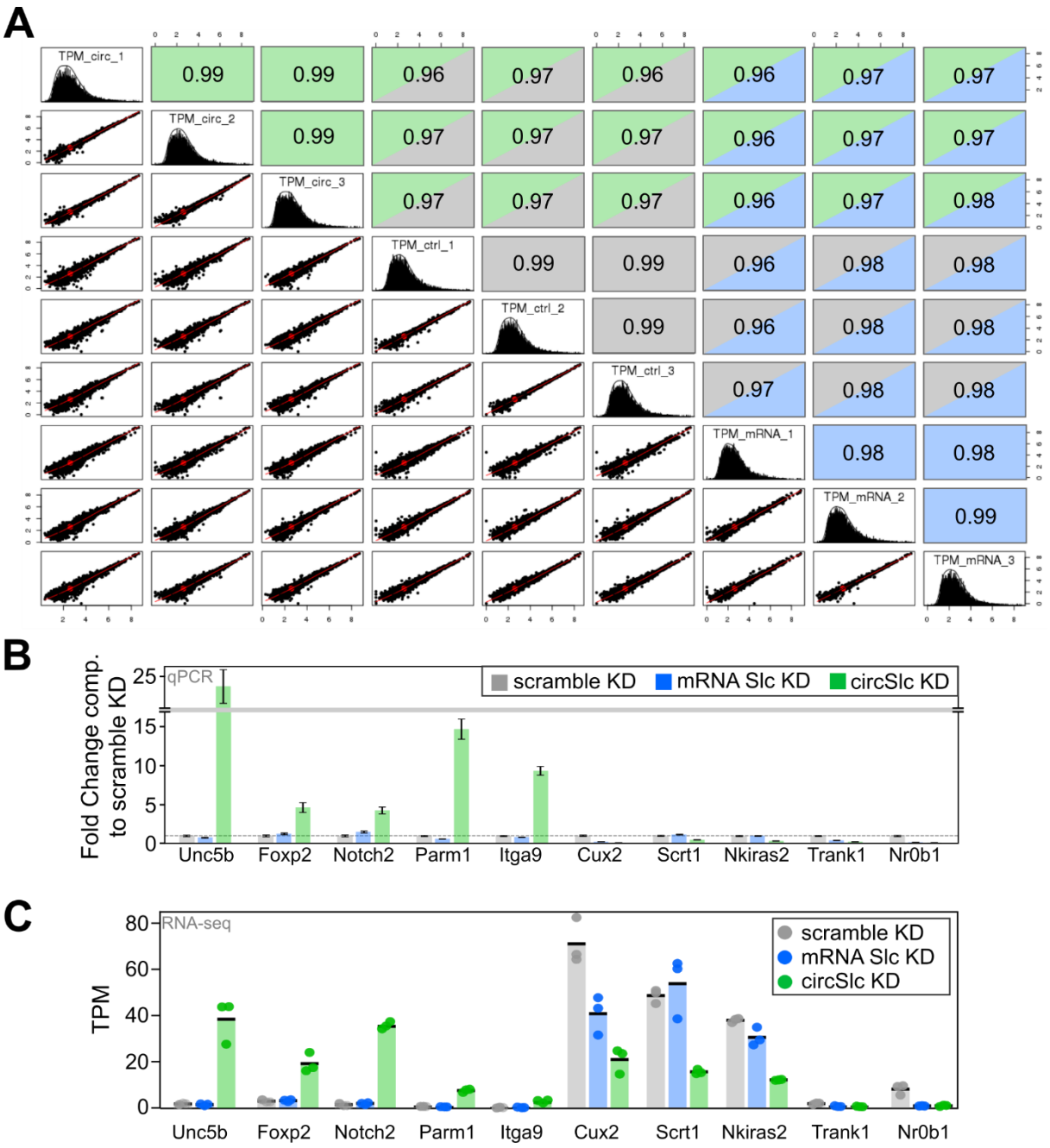

Figure S4: related to Figure 4.
(A) – Overall correlation between all biological replicates collected after knockdown of circSlc45a4, mRNA Slc45a4 and scramble KD. **(B)** – qPCR validation of induced expression changes after knockdown of circSlc45a4, mRNA Slc45a4 and scramble KD in embryonic mouse cortex. Error bars are standard error of the mean, 3 biological replicates. **(C)** – TPM (transcripts per million) values for various genes, illustrating that most changes are specific to circSlc45a4 knockdown.

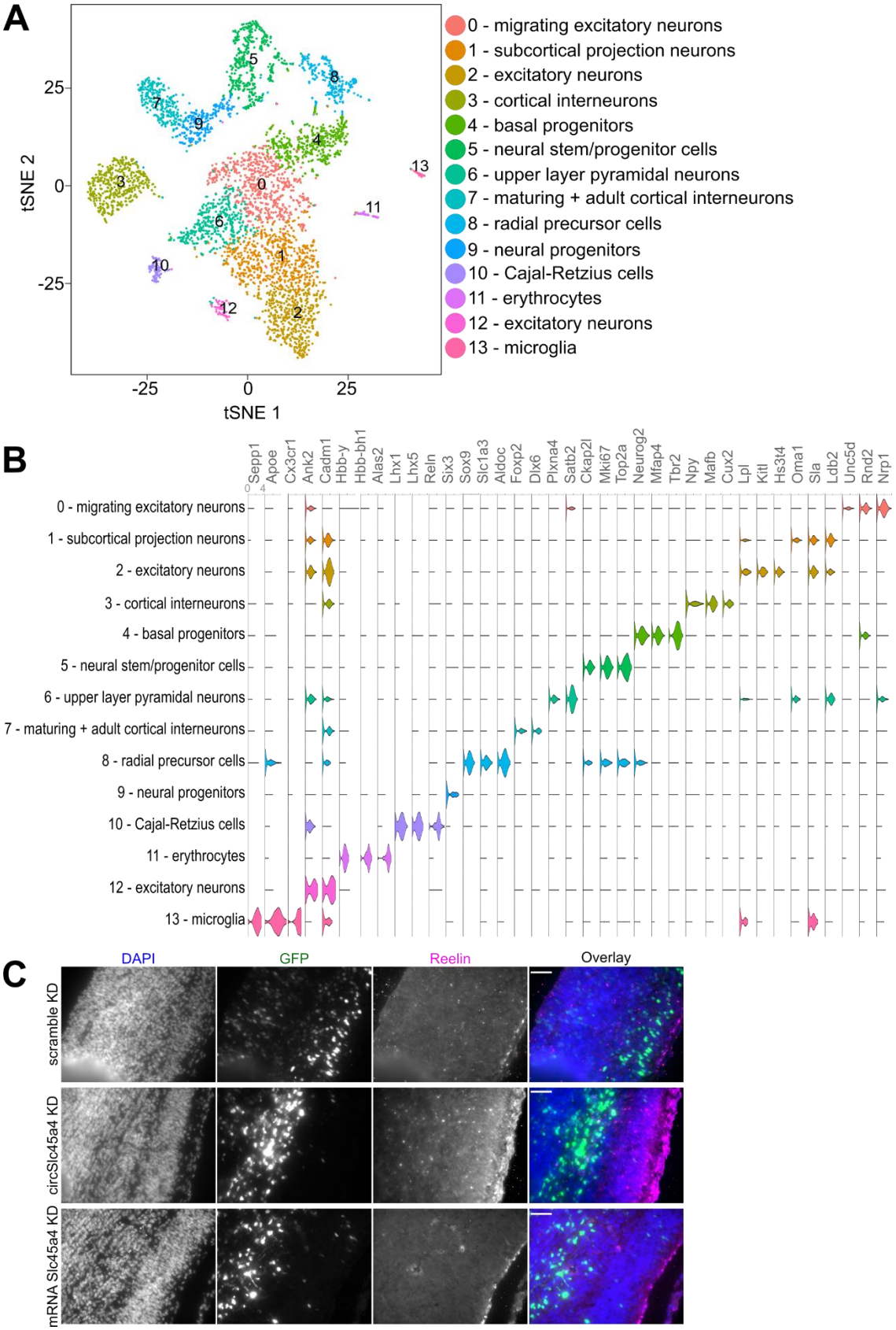

Figure S5: related to Figure 5.

(A) – tSNE plot of embryonic mouse cortex at E15.5, data from (Yuzwa et al., 2017), reanalyzed. **(B)** – Subset of identified marker genes that were used for cell population analysis. All y-scales are set from 0 to 4. **(C)** – Representative images of Reelin staining after KD of circSlc45a4, mRNA Slc45a4 and scramble KD. Scale bar is 50 µm.

Table S1, related to Figure 2: Results of GO term analysis of significantly deregulated genes after circSLC45A4 KD in SH-SY5Y

Upregulated genes					
	Term	Enrichment[1]	p-value[2]	p-adj[3]	Example genes
GO:0007156	homophilic cell adhesion via plasma membrane adhesion molecules	14/65	6.22E-10	1.24E-05	DCHS1, CELSR3, CELSR2, TRO, CADM4
GO:0098742	cell-cell adhesion via plasma-membrane adhesion molecules	15/98	2.17E-08	2.05E-04	DCHS1, CELSR3, CELSR2, TRO, CADM4
GO:0007399	nervous system development	72/1573	2.76E-07	1.26E-03	SEMA6C, GATA2, PRKCA
GO:0045652	regulation of megakaryocyte differentiation	9/40	5.14E-07	1.35E-03	SETD1A, KMT2A/B/C, TNRC6B
GO:0050808	synapse organization	18/185	1.03E-06	1.35E-03	SHANK1, L1CAM, NLGN2, BSN
GO:0034968	histone lysine methylation	12/88	2.03E-06	2.35E-03	DOT1L, KMT2A/B/C/D
GO:0016571	histone methylation	13/107	2.88E-06	2.35E-03	DOT1L, KMT2A/B/C/D
GO:0030219	megakaryocyte differentiation	9/51	4.48E-06	2.92E-03	SETD1A, KMT2A/B/C, TNRC6B
GO:0048667	cell morphogenesis involved in neuron differentiation	27/412	5.89E-06	2.98E-03	DAG1, ULK1, SEMA6C, SZT2
GO:0018022	peptidyl-lysine methylation	12/98	6.39E-06	2.98E-03	SETD1A, KMT2A/B/C, TNRC6B
GO:0048812	neuron projection morphogenesis	28/453	1.18E-05	3.01E-03	DAG1, ULK1, SEMA6C, SZT2
GO:0031175	neuron projection development	36/675	1.78E-05	3.25E-03	DAG1, SEMA6C, NCAM1, LRP1
GO:0120039	plasma membrane bounded cell projection morphogenesis	28/465	1.91E-05	3.93E-03	DAG1, SEMA6C, NCAM1, LRP1
GO:0048858	cell projection morphogenesis	28/468	2.14E-05	3.94E-03	DAG1, SEMA6C, NCAM1, NEO1
GO:0048666	neuron development	38/744	2.69E-05	4.28E-03	DAG1, SEMA6C, NCAM1, NEO1
GO:0097485	neuron projection guidance	15/171	2.86E-05	4.54E-03	DAG1, SEMA6C, NCAM1, PLXNA2
GO:0007409	axonogenesis	22/328	3.09E-05	4.54E-03	DAG1, SEMA6C, NCAM1
GO:0045814	negative regulation of gene expression, epigenetic	10/80	3.16E-05	5.28E-03	PHF1, DOT1L, HIST2H2AA3/4
GO:0061564	axon development	23/353	3.22E-05	5.43E-03	DAG1, SEMA6C, NCAM1, PLXNA2
Downregulated genes					
GO:0060087	relaxation of vascular smooth muscle	4/6	5.97E-06	0.078	GUCY1A3, PRKG1, ADORA1, RGS2
GO:0045932	negative regulation of muscle contraction	5/14	1.73E-05	0.109	GUCY1A3, PRKG1, ADORA1, PDE5A
GO:0044557	relaxation of smooth muscle	4/8	2.68E-05	0.109	GUCY1A3, PRKG1, ADORA1, RGS2
GO:0045986	negative regulation of smooth muscle contraction	4/9	4.72E-05	0.161	GUCY1A3, PRKG1, ADORA1, RGS2
GO:0006041	glucosamine metabolic process	3/4	6.44E-05	0.188	GNPDA2, GNPNAT1, PGM3

[1] number of identified genes in the entire GO term; [2] Fisher's exact test; [3] adjusted with Benjamini-Hochberg method

Table S2, related to Figure 4: Results of GO term analysis of significantly deregulated genes after circSlc45a4 KD in mouse cortex.

Upregulated genes					
	Term	Enrichment[1]	p-value[2]	p-adj[3]	Example genes
GO:0009653	anatomical structure morphogenesis	305/1578	5.00E-19	8.61E-14	Unc5b, Notch2, Pag1, Gnaq, Rbpj
GO:0023052	signaling	513/3060	5.11E-19	8.61E-14	Unc5b, Notch2, Pag1, Gnaq, Rbpj
GO:0007165	signal transduction	466/2761	1.90E-17	3.91E-13	Unc5b, Notch2, Gas7, Foxp2, Fat3
GO:0007154	cell communication	511/3097	2.10E-17	7.12E-13	Unc5b, Notch2, Ldha, Pag1, Plcb1
GO:0023051	regulation of signaling	335/1880	2.41E-15	6.67E-12	Unc5b, Notch2, Plcb1, Gnaq, Igfbp5
GO:0010646	regulation of cell communication	331/1862	5.43E-15	1.38E-11	Unc5b, Notch2, Plcb1, Nell2, Timp2
GO:0048856	anatomical structure development	517/3236	1.01E-14	1.12E-10	Unc5b, Notch2, Gas7, Foxp2, Fat3
GO:0009966	regulation of signal transduction	299/1652	1.68E-14	1.12E-10	Unc5b, Notch2, Plcb1, Sfrp2, Rbpj
GO:0007155	cell adhesion	143/635	3.53E-14	1.99E-10	Fat3, Pag1, Plcb1, Ccdc80, Cyfip2, Vcam1
GO:0035295	tube development	140/617	3.59E-14	1.99E-10	Unc5b, Notch2, Foxp2, Sfrp2, Ptges3, Gna13
GO:0022610	biological adhesion	143/637	4.61E-14	1.12E-09	Fat3, Pag1, Plcb1, Ccdc80, Cyfip2, Vcam1
GO:0032502	developmental process	546/3486	5.57E-14	1.50E-09	Unc5b, Notch2, Gas7, Foxp2, Fat3, Plcb1
GO:0051240	positive regulation of multicellular organismal process	190/937	8.67E-14	1.75E-09	Notch2, Foxp2, Plcb1, Sfrp2, Timp2, Rbpj
GO:0051094	positive regulation of developmental process	174/838	1.27E-13	8.04E-09	Notch2, Foxp2, Plcb1, Sfrp2, Timp2, Rbpj
GO:0035239	tube morphogenesis	117/491	1.60E-13	9.53E-09	Unc5b, Notch2, Sfrp2, Hs2st1, Gna13
GO:0048731	system development	433/2659	3.06E-13	9.53E-09	Unc5b, Notch2, Gas7, Foxp2, Fat3, Plcb1
GO:0032879	regulation of localization	293/1654	5.56E-13	1.07E-08	Plcb1, Gnaq, Igfbp5, Sfrp2, Nell2, Gna13
GO:0051239	regulation of multicellular organismal process	289/1626	5.58E-13	1.67E-08	Notch2, Foxp2, Fat3, Plcb1, Igfbp5, Sfrp2
GO:0007166	cell surface receptor signaling pathway	246/1332	7.36E-13	1.89E-08	Unc5b, Notch2, Usp46, Pag1, Plcb1, Gnaq
Downregulated genes					
GO:0008088	axo-dendritic transport	16/55	9.06E-06	0.094	Tmem108, Nef1, Spg7, Snapin, Ap3m2, Trak1/2
GO:0006221	pyrimidine nucleotide biosynthetic process	9/20	1.69E-05	0.094	Dut, Umps, Cad, Tyms, Dctd, Nme6, Tbpl1
GO:1901607	alpha-amino acid biosynthetic process	14/46	1.85E-05	0.094	Park7, Shmt2, Asns, Atp2b4, Cad, Adi1, Asl
GO:0006220	pyrimidine nucleotide metabolic process	10/25	2.02E-05	0.094	Dut, Umps, Cad, Tyms, Nt5c, Dctd, Nme6, Tbpl1
GO:0008652	cellular amino acid biosynthetic process	14/47	2.43E-05	0.094	Park7, Shmt2, Asns, Atp2b4, Cad, Adi1, Asl
GO:0044281	small molecule metabolic process	131/1105	5.19E-05	0.157	Eno1b, Pgm2l1, Pfkb, Abcg2, Wdtc1, Atp5o
GO:0072527	pyrimidine-containing compound metabolic process	12/39	6.49E-05	0.157	Thtpa, Dut, Umps, Cad, Tyms, Nt5c, Dctd, Nme6
GO:0019752	carboxylic acid metabolic process	72/534	6.53E-05	0.157	Dut, Tyms, Dctd, Dnph1, Shmt1

GO:0072528	pyrimidine-containing compound biosynthetic process	9/24	9.62E-05	0.201	Dut, Umps, Tyms, Dctd, Shmt1
GO:0006082	organic acid metabolic process	74/561	1.06E-04	0.201	Eno1b, Pfkb, Abcg2, Wdtc1, Cbfa2t3
GO:0006520	cellular amino acid metabolic process	32/187	1.15E-04	0.201	Park7, Arg2, Shmt2, Sars2, Asns, Gclc, Azin1
GO:0043436	oxoacid metabolic process	73/557	1.44E-04	0.201	Eno1b, Pfkp, Abcg2, Wdtc1, Cbfa2t3, Park7
GO:0009162	deoxyribonucleoside monophosphate metabolic process	5/8	2.06E-04	0.231	Dut, Tyms, Dctd, Dnph1, Shmt1
GO:0009130	pyrimidine nucleoside monophosphate biosynthetic process	5/8	2.06E-04	0.253	Dut, Umps. Tyms, Dctd, Shmt1
GO:0022616	DNA strand elongation	8/21	2.09E-04	0.253	Parp1/2, Dna2, Rad50, Rnaseh2a, Nbn, Pcna
GO:0009219	pyrimidine deoxyribonucleotide metabolic process	6/12	2.29E-04	0.253	Dut, Tyms, Nt5c, Dctd, Tbpl1, Shmt1
GO:0009157	deoxyribonucleoside monophosphate biosynthetic process	4/5	2.50E-04	0.253	Dut, Tyms, Dctd, Shmt1
GO:0009177	pyrimidine deoxyribonucleoside monophosphate biosynthetic process	4/5	2.50E-04	0.253	Dut, Tyms, Dctd, Shmt1
GO:0036265	RNA (guanine-N7)-methylation	4/5	2.50E-04	0.253	Trmt112, Mettl1, Bud23, Wdr4

[1] number of identified genes in the entire GO term; [2] Fisher's exact test, [3] adjusted with Benjamini-Hochberg method